Nano-Micro Letters

e-ISSN 2150-5551
CN 31-2103/TB

REVIEW

https://doi.org/10.1007/s40820-025-01886-y

Cite as
Nano-Micro Lett.
(2026) 18:49

Received: 6 May 2025
Accepted: 21 July 2025

Solar-Driven Redox Reactions with Metal Halide Perovskites Heterogeneous Structures

Qing Guo[1], Jin-Dan Zhang[1], Jian Li[2,3] ✉, Xiyuan Feng[4] ✉

HIGHLIGHTS

- This paper reviews the fundamentals and research progress of metal halide perovskites (MHPs)-based heterojunctions for solar-driven redox reactions.
- A comprehensive summary is presented for the construction of various MHPs-based heterojunctions (e.g., Schottky-junction, type-I/II, Z-scheme, and S-scheme).
- The versatile use of MHPs-based heterojunctions in key photocatalytic redox reactions are summarized, including H_2 evolution, CO_2 reduction, pollutant degradation, and organic synthesis.

ABSTRACT Metal halide perovskites (MHPs) with striking electrical and optical properties have appeared at the forefront of semiconductor materials for photocatalytic redox reactions but still suffer from some intrinsic drawbacks such as inferior stability, severe charge-carrier recombination, and limited active sites. Heterojunctions have recently been widely constructed to improve light absorption, passivate surface for enhanced stability, and promote charge-carrier dynamics of MHPs. However, little attention has been paid to the review of MHPs-based heterojunctions for photocatalytic redox reactions. Here, recent advances of MHPs-based heterojunctions for photocatalytic redox reactions are highlighted. The structure, synthesis, and photophysical properties of MHPs-based heterojunctions are first introduced, including basic principles, categories (such as Schottky junction, type-I, type-II, Z-scheme, and S-scheme junction), and synthesis strategies. MHPs-based heterojunctions for photocatalytic redox reactions are then reviewed in four categories: H_2 evolution, CO_2 reduction, pollutant degradation, and organic synthesis. The challenges and prospects in solar-light-driven redox reactions with MHPs-based heterojunctions in the future are finally discussed.

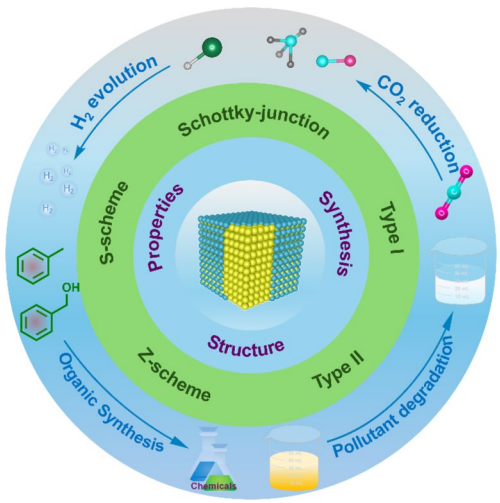

KEYWORDS Metal halide perovskite; Heterojunction; Redox reaction; Solar-to-chemical conversion

✉ Jian Li, jian.li@hzgift.org; Xiyuan Feng, fengxy@nwpu.edu.cn
[1] Xi'an Key Laboratory of Sustainable Energy Material Chemistry, Engineering Research Center of Energy Storage Materials and Devices, School of Chemistry, Xi'an Jiaotong University, Xi'an 710049, People's Republic of China
[2] Department of Physics, Zhejiang University of Technology, Hangzhou 310023, People's Republic of China
[3] Department of Physics, Gongshu Institute of Future Technology, ZJUT, Hangzhou 310022, People's Republic of China
[4] School of Microelectronics, Northwestern Polytechnical University, Xi'an 710129, People's Republic of China

Published online: 01 September 2025

1 Introduction

Owing to the advantages of mild reaction conditions and clean solar energy input, semiconductor photocatalysis technology exhibits great potential in resolving environmental concerns and energy crisis [1–5]. Semiconductor materials as the heart of photocatalytic technology have emerged in an endless stream. Metal halide perovskites (MHPs) with unique and outstanding optoelectronic properties have appeared at the forefront of semiconductor materials for photocatalysis [6]. The chemical formula of MHPs is ABX_3, where A is a monovalent metal cation (e.g., Cs^+) or an organic cation (e.g., $CH_3NH_3^+$ (MA^+), $CH(NH_2)_2^+$ (FA^+)), B is usually a divalent metal cation (e.g., Pb^{2+}, Sn^{2+}), and X is a halogen anion (e.g., Cl^-, Br^-, I^-). The divalent metal B is surrounded by six halogen ions leading to a BX_6 octahedral structure, while the A cation is in the cubo-octahedral cavity within the corner-shared BX_6 octahedral framework forming a three-dimensional (3D) structure (Fig. 1) [7–9]. Compared to traditional II-VI, III-V, and IV-VI semiconductors, MHPs possess the unique advantages as following: i) the high molar extinction coefficient of MHPs (e.g., 10^5–10^7 L mol^{-1} cm^{-1} for $CsPbX_3$ nanocrystals, ~ 10 times higher than that of CdSe with similar band gap) [10], is beneficial to the capture of solar light; ii) the optical band gaps could be facilely regulated for target reactions by quantum confinement effect or tuning compositions of anions. In combination with other striking electrical and optical properties, such as high carrier mobilities, long carrier-diffusion lengths, MHPs are considered as a promising class of candidate for photocatalytic redox reactions.

Inspired by the first photocatalytic work reported by Nam in 2016 [11], various MHP-based photocatalysts, such as $CsPbX_3$ [12–14], $Cs_3Bi_2X_9$ [15], $CsSnX_3$ [16], and $Cs_2AgBiBr_6$ [17], have been explored for solar-light-driven reactions. However, the inferior stability, severe charge-carrier recombination, and limited active sites of bare MHPs greatly restrict the photocatalytic activity and durability. Many strategies have been developed to overcome these drawbacks, such as structural and compositional modifications [18–21]. For instance, dimensionality engineering of $CsPbBr_3$ significantly boosted H_2 evolution activity [22], while alkali metal doping—despite its non-active nature—unveiled the critical role of dopant sites in charge-carrier dynamics [23]. Furthermore, facet engineering enabled precise regulation of product yield and selectivity in photocatalytic organic synthesis [24], demonstrating the versatility of MHP photocatalysts design. Particularly, construction of heterojunction has shown great potential to optimize light absorption properties and photoinduced charge-carrier dynamics. The concept of heterojunction was first proposed in semiconductor physics by W. Shockley [25]. According to definition, heterojunctions are constructed by two or more semiconductors with similar crystal structures, coefficient of thermal expansions, and unequal band structure via physical or chemical bonding. Driven by built-in electric field at the interface, photogenerated electrons and holes could be spontaneously oriented and expedited transfer toward opposite direction, thus achieving much better photocatalytic performance than that of individual semiconductors [26]. To date, many MHPs heterojunctions have been developed and verified the effectiveness of heterojunction engineering on photocatalytic performance by enhancing light absorption ability, passivating surface, and promoting charge-carrier dynamics of MHPs. However, to the best of our knowledge, little attention has been paid to the summary of MHPs-based heterojunctions for photocatalytic redox reactions. A comprehensive and timely review concerning this field is highly desired, which will be significant for the design of future effective photocatalysts to realize solar-to-chemicals conversion.

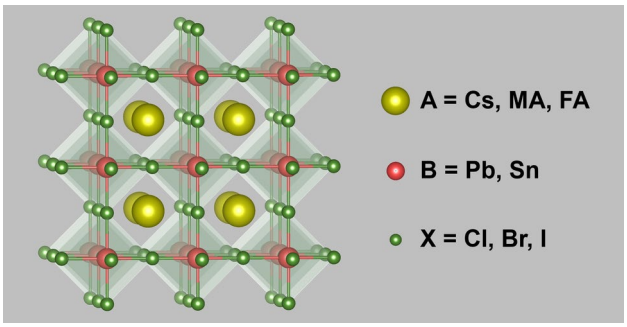

Fig. 1 3D structure of MHPs

This current review presents the recent progress of MHPs-based heterojunctions for photocatalytic redox reactions, as shown in Fig. 2. We first briefly introduce the structure, preparation methods, and photophysical properties of representative MHPs-based heterojunctions. Then, recent advances of MHPs-based heterojunctions in various photocatalytic redox reactions for improved photocatalytic performance and stability are introduced in terms of H_2 evolution, CO_2 reduction, pollutant degradation as well as organic synthesis. Finally, we present the possible challenges and prospects in this exciting field.

https://doi.org/10.1007/s40820-025-01886-y

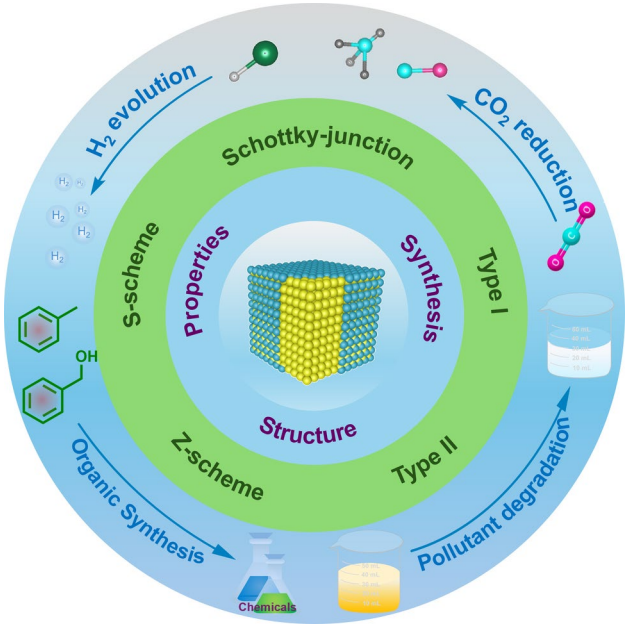

Fig. 2 Schematic illustration of the full structure of this manuscript: type of heterojunction, the preparation methods, and the applicable reactions

This review gives the readers a clear picture about MHPs-based heterojunctions and provides guidance for designing advanced MHPs-based photocatalysts.

2 Basic Principles, Categories, and Synthesis of MHPs-Based Heterojunctions

The structure of heterojunctions plays a key role in photocatalytic performance. In the following part, the basic principles, categories, and typical synthesis methods of MHPs-based heterojunctions will be outlined.

2.1 Basic Principles of Heterojunction Photocatalysts

In general, photocatalysis involves (Fig. 3a) [27–29]: (i) light absorption and generation of charge carriers (with the efficiency of η_{LH}), in which the incident photon energy ($h\nu$) is equal to or larger than the band gap (Eg) of the semiconductors; (ii) separation of photogenerated charge carriers to produce electrons in the conduction band (CB) and holes in the valence band (VB) of semiconductors (with the efficiency of η_{col}); (iii) redox reactions on active sites (with the efficiency of η_{cat}) with electrons and holes in CB and VB as reductant and oxidant. To enable charge carriers to drive corresponding redox reactions, suitable band-position alignment of semiconductors should be considered to meet the thermodynamic requirements. The bottom of CB should be more negative than the reduction potential of electron acceptors (A, such as H^+, CO_2, and so on), while the top of VB should be more positive than the oxidation potential of electron donors (D, such as sacrificial reagent, R-OH, and OH^-) (Fig. 3b). However, photogenerated electrons and holes would be depleted with a seriously radiative recombination because of the extremely strong Columbic force between electrons and holes, and non-radiative annihilation at trap states in the form of emitted light and heat, respectively.

Based on the above mechanism, the recombination of electron–hole pairs in the bulk or on the surface of photocatalysts would be competitive to the desired redox reactions, which is detrimental to photocatalytic performance. Construction of heterojunctions with intimate interfaces provides a promising approach to effectively separate the electron–hole pairs for redox reactions [30–32]. According to the alignment of energy levels and charge-transfer models, the reported MHPs-based heterojunctions can be

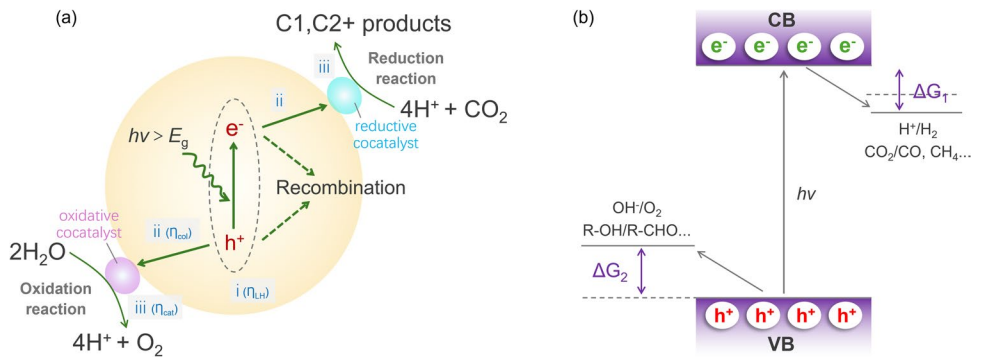

Fig. 3 **a** General photocatalytic reaction process. **b** Energy diagram for photocatalytic reaction

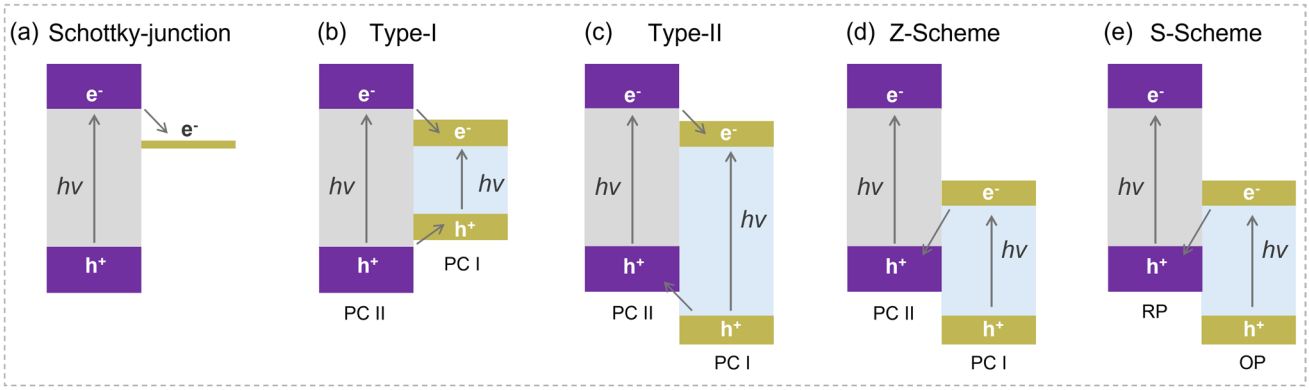

Fig. 4 Schematic illustration of the band alignment and charge migration pathways in Schottky junction, Type-I, Type-II, Z-Scheme, and S-Scheme heterojunctions

divided into five types, including: (i) Schottky junction, (ii) Type-I, (iii) Type-II, (iv) Z-scheme, and (v) S-scheme (Fig. 4). It will be discussed in detail in the following section.

2.2 Categories of MHPs-Based Heterojunction Photocatalysts

In the past decades, considerable efforts have been made on the design and fabrication of heterojunctions to improve photocatalytic performance of MHPs. Overall, there are five typical categories of heterojunction photocatalysts, including: (i) Schottky junction, (ii) Type-I, (iii) Type-II, (iv) Z-scheme, and (v) S-scheme. The design principle will be discussed in detail in the following.

2.2.1 Schottky Junction

A Schottky junction is formed via the intimate contact of MHPs with a metal. Taking metal/n-type semiconductor as an example (Fig. 5) [32, 33], the differences in work functions (W) or Fermi level (E_F) promote the free electrons transfer at the interface between the metal and semiconductor. When the Fermi level of semiconductor ($(E_F)_s$) is higher than that of metal ($(E_F)_m$), free electrons would flow from semiconductor to metal until the Fermi levels reach the same position, leading to the band bending and the formation of Schottky barrier. The back flow of electrons is effectively prevented by the Schottky barrier, and the high work function of metal provides a high driving force to transfer electrons to the adsorbed molecules. Under light irradiation, photogenerated electrons from the CB of MHPs would rapidly transfer to the metals to participate in the reduction reactions, while holes left in VB of MHPs would be consumed through oxidation reactions. On the contrary, when the Fermi level of semiconductor ($(E_F)_s$) is lower than that of metal ($(E_F)_m$), the electrons would transfer from metal to semiconductor, leading to the accumulation of electrons near semiconductor surface. Obviously, the lower $(E_F)_m$ than $(E_F)_s$ promotes the separation and transfer of photogenerated electron–hole under light irradiation, resulting the improved photocatalytic performance. For example, the loaded metal Pt with the highest work function (5.7 eV) and lowest Fermi level promoted H_2 evolution activity of $MAPbBr_{3-x}I_x$ with ~ 3-time enhancement [34].

Few-layered metal chalcogenides (e.g., WS_2) [35], transition metal carbide (e.g., Ti_3C_2) [36, 37], and carbon-based materials with good metallic conductivity, were also hybridized with MHPs to form a Schottky junction, like the semiconductor–metal heterojunction system. Benefiting from the following properties: (i) as a good electron acceptor and transfer channel, promoting electron–hole pairs separation [38], and (ii) large specific surface areas, providing sufficient active reaction sites, the formed Schottky junctions boost the photocatalytic performance of MHPs. For example, γ-$CsPbI_3$ NCs hybridized with few-layered WS_2 nanosheets exhibited a significant enhancement in photocatalytic methylene blue (MB) degradation, attributed to the increased amount of γ-$CsPbI_3$ NCs and the superior carrier-transport property of few-layered WS_2 nanosheets [35]. Moreover, DFT calculations on $Ni_3C/MAPbI_3$ revealed how metal work functioned and Fermi level alignment facilitated electron extraction and reduced recombination [39].

https://doi.org/10.1007/s40820-025-01886-y

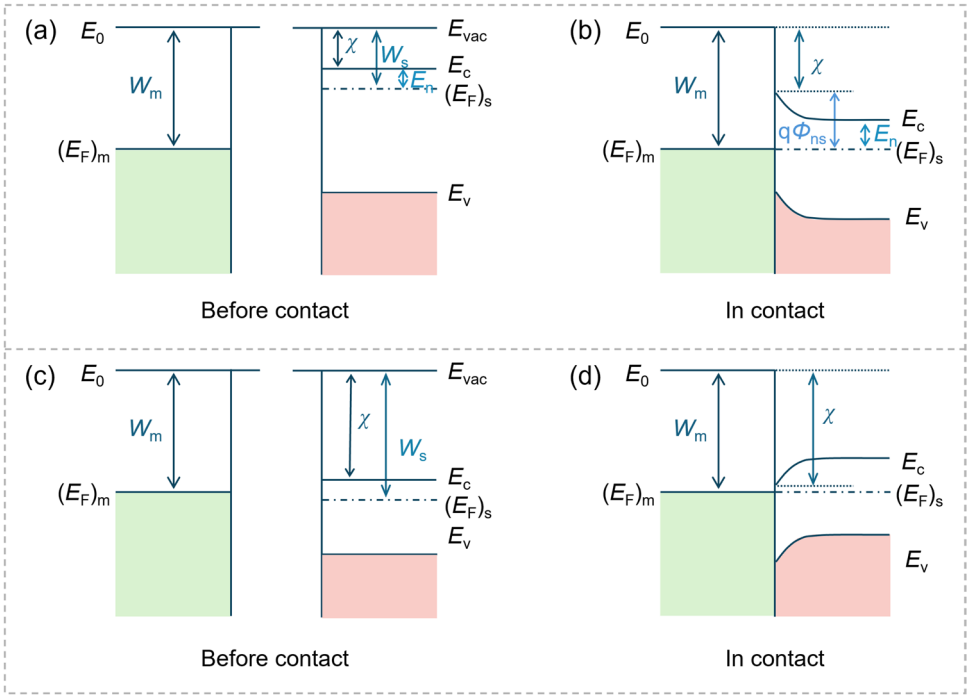

Fig. 5 Schematic illustration of the energy band alignment of metal and n-type semiconductor contacts toward $W_m > W_s$ **a** and **b**, and $W_m < W_s$ **c** and **d**. E_{vac}, vacuum energy; E_c, energy of conduction band minimum; E_v, energy of valence band maximum; W_m, metal work function; W_s, semiconductor work function; χ, electron affinity of the semiconductor

2.2.2 Type-I Heterojunction

The type-I heterojunction is formed by two coupled semiconductors (i.e., photocatalysts I and II) with straddling band structures. The CB energy potential of photocatalyst I (PC I) is lower than that of photocatalyst II (PC II), while VB potential of PC I is higher than that of PC II (Fig. 4b). Under light irradiation, the photogenerated electrons and holes in PC II would transfer to the CB and VB of PC I, respectively, resulting in the accumulation of both electrons and holes in PC I (Fig. 6a). Obviously, efficient spatial separation of photogenerated electron–hole pairs cannot be realized and the redox potentials of the heterojunction photocatalysts will be decreased, since both reduction and oxidation reactions occur on PC I with narrower bandgap [40]. However, the surface of PC I can be passivated with PC II, and more active sites would be exposed. For example, the constructed type-I heterojunction $CsPbBr_3/Cs_4PbBr_6$ enhanced CO_2 photoreduction activity toward CO [41]. In addition, MHPs nanocrystals immobilized on two-dimensional (2D) black phosphorus (BP) nanosheets promoted CO_2 conversion rate because the introduced BP could offer more active sites for CO_2 activation [42].

2.2.3 Type-II Heterojunction

One of the most popular heterojunctions is type-II, in which the CB and VB energy positions of PC II are higher than those of PC I with the staggered band structure (Fig. 4c). Upon light irradiation, photogenerated electrons on the CB of PC II with a higher reduction potential could transfer to PC I and holes in PC I with stronger oxidation ability would simultaneously transfer to PC II. Correspondingly, electron and hole wave functions can be preferentially localized in PC I and PC II, respectively (Fig. 6b) [43]. The decreased electron–hole overlap prolongs the lifetime of the exciton while decreases the exciton spin relaxation rate and non-radiative recombination, leading to effective spatial separation of photogenerated electron–hole pairs. Besides, the staggered band arrangement can extend the light absorption range through indirect transition between the two different materials' energy levels [44]. The above properties enable MHPs-based type-II structure widely used in photocatalytic field. For example, the photocatalytic C(sp^3)-H transformation activity of $Cs_3Bi_2Br_9$/CdS heterojunction was much greater than those of bare $Cs_3Bi_2Br_9$ and CdS owing to the staggered band structure [45], revealed by DFT calculations.

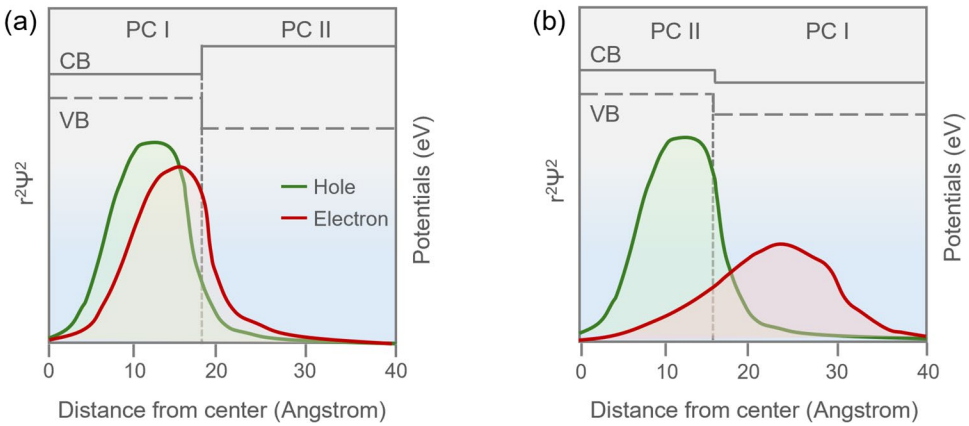

Fig. 6 Schematic of radial distribution function of lowest energy conduction band (CB) electrons (red traces) and valence band (VB) holes (green lines) in **a** type-I and **b** type-II heterojunctions

Similarly, the in situ prepared Cs_2SnI_6/SnS_2 showed a superior CO_2 photoreduction to CO because of the ultrafast carrier separation and prolonged lifetime of electrons [21].

2.2.4 Z-Scheme Heterojunction

Although the charge-carrier separation can be promoted by type-II heterojunctions, the redox ability of photogenerated electron–hole is greatly weakened. In addition, from a dynamic perspective, the repulsion from the existing electrons in PC I will hinder the continuous transfer of electrons from PC II, impeding the realization of spatial charge separation. To overcome these drawbacks, the Z-scheme heterojunction has been introduced (Fig. 4d). According to composition, Z-scheme could be classified into three different structures [43, 46–48]: (i) PS-A/D-PS (Fig. 7a) with ionic redox pairs as ionic electron mediator (electron acceptor/donor pair known as A/D pair); (ii) all-solid-state Z-scheme with a solid conductor (e.g., metal, carbon nanotubes, graphene) as the mediator (Fig. 7b), and (iii) direct Z-scheme without mediator (Fig. 7c). MHPs-based Z-scheme junctions are mainly the last two structures. Under light irradiation, photogenerated electrons in CB of PC I would recombine with holes in the VB of PC II through the mediator with a low contact resistance interface. The solid conductor greatly shortens the distance of electron flow from PC I to PC II and renders a more promising electron relaying ability. For direct Z-scheme, the solid–solid contact interface allows Z-schematic vectorial electron transfer between semiconductors. The electrons in PC I would shuttle to PC II and combine with holes in PC II driven by strong electrostatic attraction

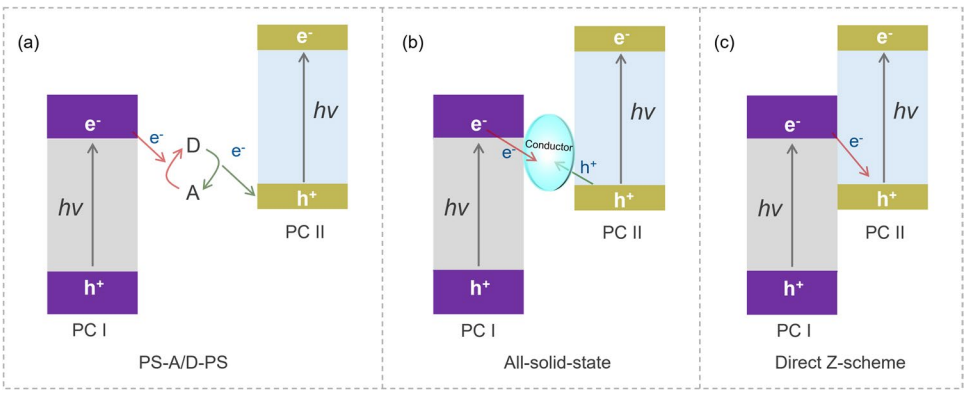

Fig. 7 Illustration of three kinds of Z-scheme heterojunction structures, **a** PS-A/D-PS, **b** all-solid-state, and **c** direct Z-scheme

https://doi.org/10.1007/s40820-025-01886-y

between opposite charge clouds. Meanwhile, photoexcited holes in PC I and electrons in PC II would stay still because of the electrostatic repulsion. As a result, the photogenerated electrons and holes accumulate at the high potential to realize spatial separation and strong redox ability simultaneously. Taking advantage of this merit, Xu et al. constructed $Cs_2AgBiBr_6$@g-C_3N_4 Z-scheme system in toluene through an in situ assembly method to enhance CH_4 generation and selectivity in photocatalytic CO_2 reduction [49].

2.2.5 S-Scheme Heterojunction

Recently, S-scheme (or Step-scheme) heterojunction has been proposed, which consisted of RP (reduction photocatalyst with high CB) and OP (oxidation photocatalyst with low VB) with staggered band structure (Fig. 8a), like type-II heterojunction but with a different charge transfer route [50–52]. When they are in close contact (Fig. 8b), electrons in RP would spontaneously diffuse to OP, leading to the formation of electron depletion layer and electron accumulation layer in the interface of RP and OP, respectively. Consequently, an internal electric field directing from RP to OP would be created. Upon light irradiation (Fig. 8c), the band bending will drive the photogenerated electrons in the CB of OP and holes in the VB of RP to recombine at the interface. Photogenerated holes are reserved in the VB of OP and electrons are reserved in CB of RP, which makes the heterojunction have the highest oxidation–reduction capacity. For example, a fabricated 2D/2D $BiVO_4$/$CsPbBr_3$ S-scheme heterojunction through an in situ face-to-face grown strategy featured desirable accelerated dynamic carrier mobility, achieving high CO_2-to-CO conversion with a turnover number (TON) near 230 without any co-catalyst or sacrificial agent [53]. DFT calculations revealed that such enhancement was attributed to the built-in electric fields and band bending in interfacial.

2.3 Strategies for Building MHPs-based Heterojunction Photocatalysts

The rational design and synthesis of MHPs-based heterojunctions is of importance for photocatalytic performance. Various methods have been developed to fabricate MHPs-based heterojunction structures. Common preparation methods of MHPs-based heterojunction photocatalysts are summarized into the following four types.

2.3.1 Physical Mixing Method

Physical mixing is the simplest method to construct MHPs-based heterojunctions. In a typical procedure, the as-prepared MHPs were mixed with an appropriate amount of heteromaterials in solution and then ultrasonicated or stirred to allow the full hybridization through weak van der Waals interaction. Employing this simple and facile method, Bi_2WO_6 [54], P3HT conducting polymer [55], BiOBr [56], AgBr [57], Ti_3C_2 [37], and other materials [58, 59] were decorated onto MHPs to construct MHPs-based heterojunctions for solar-light-driven redox reactions.

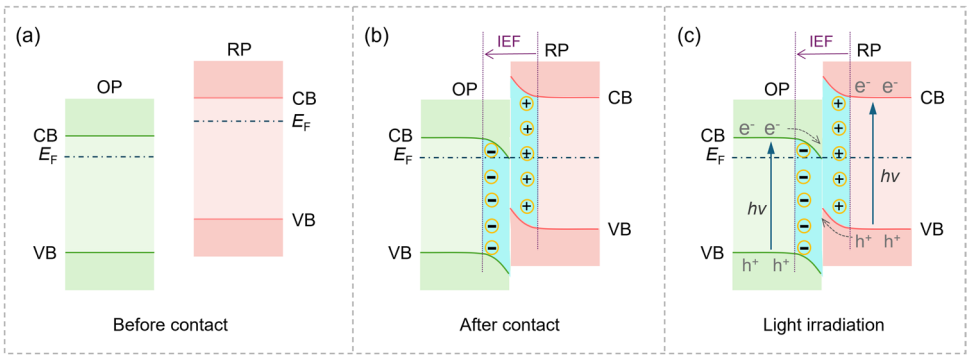

Fig. 8 Schematic illustration of S-scheme heterojunction: internal electric field (IEF)-induced charge transfer, separation, and the formation of S-scheme heterojunction under light irradiation

2.3.2 Electrostatic Self-Assembly Method

Because of the weak van der Waals interaction, charge transfer only takes place when a free collision occurs, making the charge transfer random and inefficient. In this regard, an electrostatic self-assembly approach was developed to form intimate contact [16, 39]. For this process, the electrostatic interaction between oppositely charged semiconductors provided the driving force. For instance, 2D/2D $CsPbBr_3$/BiOCl heterojunction was fabricated through electrostatic self-assembly of positively charged $CsPbBr_3$ with Zeta-potentials of 17.8 mV and negatively charged BiOCl with Zeta-potential of -10.4 mV [60]. Because of the opposite charge on the surface, the assembly of $CsPbBr_3$ and BiOCl would be spontaneous via electrostatic interaction. Similarly, positively charged $CsPbBr_3$ was immobilized onto the negatively charged covalent triazine frameworks to fabricate type-II heterojunction for photocatalytic CO_2 reduction to CO [61].

2.3.3 In situ Growth Method

In situ growth means that the as-prepared material is used as the substrate for the subsequent growth of another material or simultaneous growth of two materials in their mixed precursor solutions. According to the growth sequences, we classified this method into the following three types in detail.

Addition of heteromaterials into MHPs precursor solution: The heterojunction can be built by the growth of MHPs on the as-prepared heteromaterials. For instance, Li et al. applied in situ hot-injection method to synthesize $CsPbBr_3$-CdZnS NRs heterojunction for CO_2 photoreduction [62]. The strong affinity between S and Pb atoms enabled the pre-adsorption of Pb^{2+} on CdZnS. Cs precursor was then injected into the above mixture to grow $CsPbBr_3$ onto CdZnS to form type-II $CsPbBr_3$-CdZnS heterojunction. $FAPbBr_3/Bi_2WO_6$ composite was also prepared by the antisolvent precipitation method, in which the precursor solution of $FAPbBr_3$ was added dropwise to the suspension of as-prepared Bi_2WO_6 [63]. A mechanochemical synthesis with ball milling was also reported to grow MHPs onto heteromaterials. For example, $DMASnBr_3$@g-C_3N_4 composite was constructed by adding g-C_3N_4 into DMABr and $SnBr_2$, which were charged under inert atmosphere in a jar and milled for several hours [64].

Addition of MHPs into heteromaterials precursor: The heterojunctions are built by the growth of other semiconductors onto MHPs. To prepare $CsPbBr_3$@ZIFs, the as-prepared $CsPbBr_3$ QDs were first dispersed into ethyl acetate solution, and zinc acetylacetonate along with 2-methylimidazole was then added with constant stirring for ZIF growth [65]. In this process, the assistance of light, microwave, or thermal was usually introduced. For instance, Pt-SA/$CsPbBr_3$ hybrid NCs were obtained through the introduction of monodisperse $CsPbBr_3$ NCs into Pt precursor (platinum(II) bis-(acetylacetonate)) under light irradiation [66]. To synthesize $CsPbBr_3$@GDY hybrid [67], the as-prepared $CsPbBr_3$ nanocrystals as a growth substrate were mixed with hexamethylbenzene monomer in a microwave reactor. $CsPbCl_3/W_{18}O_{49}$ composites were prepared by adding $CsPbCl_3$ to WCl_6 propanol solution through hydrothermal methods [68].

Mixing of precursors of MHPs and heteromaterials: The construction of heterojunctions which share the same metal by the two materials involves the mixing of precursors of MHPs and heteromaterials, such as the synthesis of $MA_3Bi_2I_9/DMA_3BiI_6$ heterojunction [69]. In detail, the precursors including MAI, $Bi(NO_3)_3$, and HI were mixed and then transferred into a Teflon-lined stainless-steel autoclave for a solvothermal route. Employing this method, 0D $CsPbBr_3$/2D $CsPb_2Br_5$ was also developed by hot injection using $PbBr_2$ and Cs_2CO_3 as precursors [70]. Obviously, this approach ensures tight interfacial contact because of the formation of strong chemical bond between two materials, leading to effectively promoted charge-carrier dynamics.

2.3.4 Hybrid Strategies

To develop MHPs-based heterojunction photocatalysts with abundant properties, the above-mentioned strategies are usually combined collaboratively. For example, in situ growth was combined with physical mixing strategy to develop a ternary heterojunction material bismuth perovskite-TiO_2-Ru(II) polypyridyl (CBB/TiO_2/RuPS) [71]. In detail, CBB was first synthesized via ligand-assisted solvent reprecipitation method. TiO_2 was then deposited onto CBB to obtain CBB/TiO_2 by in situ hydrolysis. RuPS was finally anchored

 https://doi.org/10.1007/s40820-025-01886-y

onto TiO_2 shell by physical mixing of as-prepared RuPS and CBB/TiO_2 in methanol under inert atmosphere. $CsPbBr_3$/USGO/α-Fe_2O_3 hybrids were also constructed using in situ growth combining with electrostatic self-assembly approach [72]. However, it is still challenging for hybrid strategies, since multiple materials must be integrated in one at nanometer scale.

3 MHPs-Based Heterojunctions for Solar-Light-Driven Redox Reactions

In recent years, solar-light-driven redox reactions by MHPs-based heterojunctions have achieved rapid development. In this part, we will discuss the progress of MHPs heterojunctions in terms of photocatalytic H_2 evolution, CO_2 reduction reaction, organic pollutant degradation, and organic synthesis reaction.

3.1 MHPs-Based Heterojunctions for Photocatalytic H_2 Evolution

Hydrogen (H_2) with high-energy density and environmental benignity is considered as an ideal energy carrier to replace traditional fossil fuels [73, 74]. Solar-light-driven water splitting is a promising approach to produce renewable H_2, in which solar energy is converted to chemical energy with two main redox processes, water oxidation for oxygen evolution and proton reduction for hydrogen evolution [75, 76]. However, it is still challenging to use MHPs as photocatalysts to generate H_2 from water splitting, because of their ionic nature and poor stability in water. To overcome this issue, hydrohalic acid (HX) splitting as an alternative strategy was adopted for photocatalytic H_2 evolution. In this strategy, MHPs were stabilized through a dynamic precipitation–solubility equilibrium in saturated HX solution. Compared to the four-electron water splitting, only two electrons were involved for HX splitting and the potential of X^- oxidation (e.g., $E_{I3-/I-} = 0.53$ V *vs.* NHE, pH = 0) was much lower than that of water oxidation ($E_{O2/H2O} = 1.23$ V *vs.* NHE, pH = 0). Table 1 summarizes the typical examples of H_2 generation based on MHPs-based heterojunction photocatalysts.

3.1.1 *Schottky Junctions for Photocatalytic H_2 Evolution*

The first work on MHPs-based heterojunction for H_2 evolution was reported in 2016 by Nam and coworkers [11], in which Pt nanocrystals were loaded on $MAPbI_3$ via in situ photoreduction. The modification of Pt not only formed a Schottky junction, but also acted as a cocatalyst for proton reduction. The resulting $MAPbI_3$/Pt showed a 1.8-fold enhancement for H_2 evolution activity. Following this pioneering work, Pt nanoparticles and single atoms were widely decorated to construct Schottky junction with MHPs [34]. Because of serious environmental issues, the lead-free MHPs were recently developed to construct Schottky junction, such as $(CH_3NH_3)_3Bi_2I_9$/Pt [87], and PtSA/Cs_2SnI_6 [77], to improve photocatalytic H_2 evolution activity (Fig. 9).

Besides, the materials with metallic character were also incorporated to construct Schottky junctions to improve photocatalytic H_2 evolution. For example, Ni_3C/$MAPbI_3$ photocatalyst was synthesized by a facile surface charge-promoted self-assembly route (Fig. 10a) [39]. Owing to the improved charge-carrier transfer and separation as well as the massive reactive centers, the optimal Ni_3C/$MAPbI_3$ photocatalyst (2362 μmol g^{-1} h^{-1}) showed almost 55-fold improvement of H_2 generation rate in HI saturated aqueous solution (Fig. 10b, c) compared to pristine $MAPbI_3$ (43 μmol g^{-1} h^{-1}). Likewise, Min et al. obtained $MAPbI_3$/$Ti_3C_2T_x$ through in situ integration of $MAPbI_3$ microcrystals with $Ti_3C_2T_x$ NSs [37]. The optimal $MAPbI_3$/$Ti_3C_2T_x$ hybrid exhibited a 43-fold enhancement of H_2 evolution rate relative to that of pure $MAPbI_3$. More importantly, a stable H_2 evolution activity over a 120-h reaction period was achieved, due to the interfacial passivation effect of $Ti_3C_2T_x$. CoP with excellent conductivity was also reported to construct $MAPbI_3$/CoP Schottky junctions to boost photocatalytic H_2 evolution performance of MHPs (Fig. 10d-f) [78].

3.1.2 *Type-I Heterojunctions for Photocatalytic H_2 Evolution*

Type-I heterojunctions were constructed by coupling MHPs and heteromaterials with suitable band alignment to facilitate H_2 evolution. Chen et al. anchored 2D few-layer black phosphorus (BP) on $MAPbI_3$ via electrostatic coupling to

Table 1 A summary of the photocatalytic activity of the representative MHPs-based heterojunctions in H_2 evolution

Photocatalysts	Hetero-junction	Reaction solution	Electron donor	Light source	H_2 generation rate	AQY (%)	Refs
PtSA/Cs_2SnI_6	Schottky junction	HI/H_3PO_2	HI	300 W Xe lamp, > 420 nm	430 μmol h^{-1} g^{-1}	/	[77]
$MAPbBr_{3-x}I_x$/Pt	Schottky junction	HI/HBr/H_3PO_2	HI	300 W Xe lamp, > 420 nm	2604.8 μmol h^{-1} g^{-1}	8.10 (450 nm)	[34]
$MAPbI_3$/CoP	Schottky junction	HI/H_3PO_2	HI	300 W Xe lamp, > 420 nm	785.9 μmol h^{-1} g^{-1}	/	[78]
Pt-DA_3BiI_6	Schottky junction	DAI/HI/H_3PO_2	HI	white LED lamp	57 μmol h^{-1} g^{-1}	0.83 (535 nm)	[79]
$Cs_2AgBiBr_6$/N–C-140	Schottky junction	HBr/H_3PO_2	HBr	300 W Xe lamp, > 420 nm	380 μmol g^{-1} h^{-1}	0.59 (420 nm)	[80]
$MAPbI_3$-$Ti_3C_2T_x$	Schottky junction	HI/H_3PO_2	HI	white LED lamp	578.2 μmol h^{-1} g^{-1}	/	[37]
$MAPbI_3$/rGO	Schottky junction	HI/H_3PO_2	HI	300 W Xe lamp, > 420 nm	894.3 μmol h^{-1} g^{-1}	1.5 (450 nm)	[81]
Ni_3C/$MAPbI_3$	Schottky junction	HI/H_3PO_2	HI	300 W Xe lamp, > 420 nm	2362 μmol g^{-1} h^{-1}	16.6 (420 nm)	[39]
BP/$MAPbI_3$	Type-I	HI/H_3PO_2	HI	300 W Xe lamp, > 420 nm	3742 μmol h^{-1} g^{-1}	23.2 (420 nm)	[82]
$Cs_3Bi_2Br_9$/g-C_3N_4	Type-II	Water/triethanolamine	Triethanolamine	1500 W Xe lamp, 300–800 nm	1050 μmol g^{-1} h^{-1}	/	[83]
$MA_3Bi_2I_9$/DMA_3BiI_6	Type-II	HI/H_3PO_2	HI	300 W Xe lamp, > 420 nm	198.2 μmol h^{-1} g^{-1}	/	[69]
ML-MoS_2/$MAPbI_3$-MC	Type-II	HI/H_3PO_2	HI	300 W Xe lamp, > 420 nm	3.6 mmol g^{-1} h^{-1}	11.6 (450 nm)	[84]
Pt/TiO_2-$MAPbI_3$	Type-II	HI/H_3PO_2	HI	300 W Xe lamp, > 420 nm	1986.7 μmol h^{-1} g^{-1}	70 (420 nm)	[85]
$DMASnBr_3$@g-C_3N_4	Type-II	Water/triethanolamine	Triethanolamine	1500 W Xe lamp, 300–800 nm	18.6 μmol g^{-1} h^{-1}	/	[64]
V_{Br}-$Cs_2AgBiBr_6$/WO_3	S-scheme	HBr/H_3PO_2	HBr	300 W Xe lamp, > 420 nm	364.89 μmol g^{-1} h^{-1}	/	[86]

obtain a type-I heterojunction (Fig. 11) [82]. The mechanism insights indicated that BP not only extracted electrons from $MAPbI_3$ through a type-I heterojunction, but also provided abundant active sites for proton reduction reaction. As a result, the BP/$MAPbI_3$ composite yielded a superior H_2 generation rate of 3742 μmol h^{-1} g^{-1}. Because the electrostatic adsorbed BP on the surface of $MAPbI_3$ resulted in interfacial passivation, the composite showed an excellent stability in HI solution. The lead-free MHPs were also adopted to form type-I heterojunction, because of their environmentally friendly behavior. For example, Zhao et al. synthesized NiCoP/$Cs_2AgBiBr_6$ (NCP/CABB) via a simple electrostatic adsorption method [88]. Benefiting from the broadened visible light absorption range and promoted photoelectrons transfer, NCP/CABB achieved an 88-time improvement of H_2 generation.

3.1.3 Type-II Heterojunctions for Photocatalytic H_2 Evolution

Owing to the efficient charge-carrier spatial separation, type-II heterojunction has aroused great attention for enhanced photocatalytic H_2 production. Zhao et al. anchored small-sized monolayer MoS_2 nanosheets (ML-MoS_2), onto large-sized $MAPbI_3$ microcrystal ($MAPbI_3$-MC) to construct type-II heterojunction $MAPbI_3$-MC/ML-MoS_2 [84]. The surface photovoltage differences in Kelvin probe force microscopy directly confirmed the effective spatial separation of the photogenerated electrons and holes, and the existence of strong built-in electric field aligned between $MAPbI_3$-MC (oxidation site) and ML-MoS_2 (reduction site) (Fig. 12a, b). A superior H_2 production rate of 13.6 mmol g^{-1} h^{-1} was achieved under visible light (Fig. 12c). $MoSe_2$ has also been reported to couple with $MA_{1-x}FA_xPbI_3$ to construct type-II heterojunction for enhanced H_2 evolution [89]. Similarly, a

https://doi.org/10.1007/s40820-025-01886-y

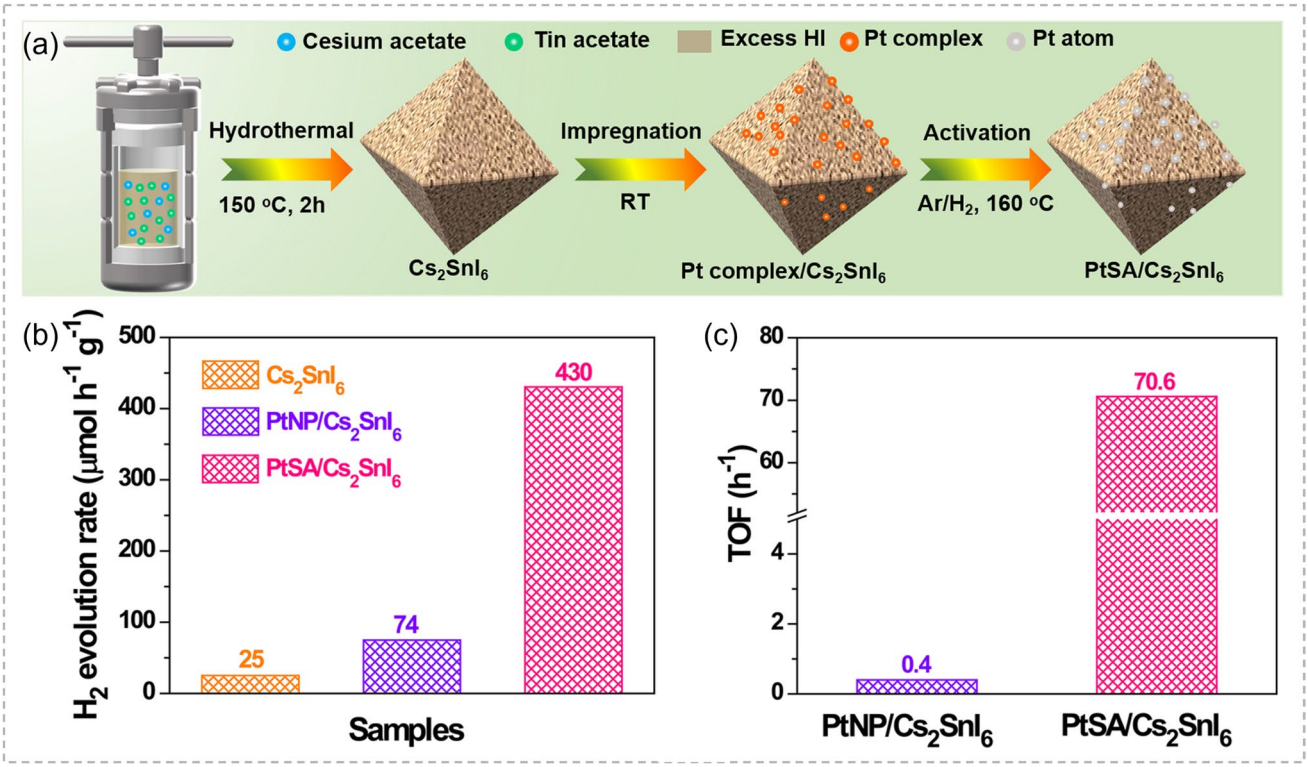

Fig. 9 **a** Schematic illustration of $PtSA/Cs_2SnI_6$ preparation process. **b** Photocatalytic H_2 generation rate over $PtSA/Cs_2SnI_6$, $PtNP/Cs_2SnI_6$, and Cs_2SnI_6 catalysts, and **c** the corresponding TOF values of $PtSA/Cs_2SnI_6$ and $PtNP/Cs_2SnI_6$ catalysts. Reproduced with permission [77]. Copyright 2020, Springer Nature

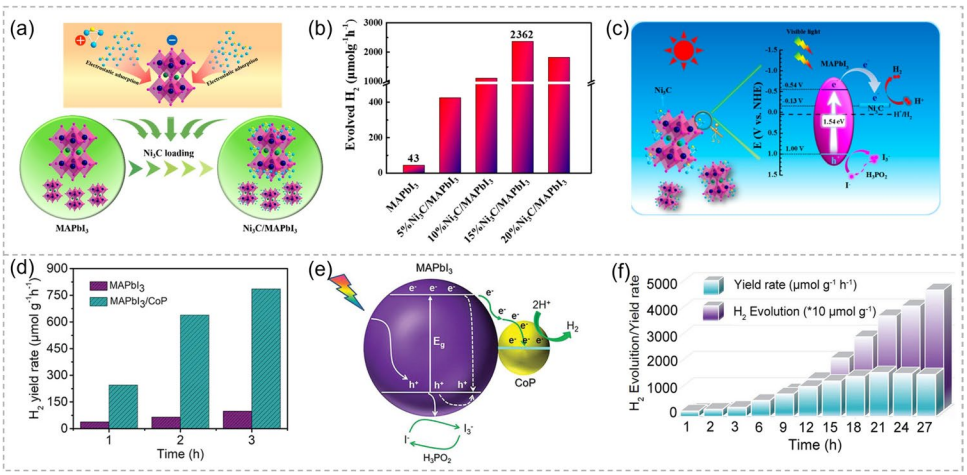

Fig. 10 **a** Schematic illustration of synthesis process of $Ni_3C/MAPbI_3$ photocatalyst, **b** photocatalytic H_2 evolution performance under light irradiation, and **c** band diagram of $Ni_3C/MAPbI_3$ for HI splitting reaction. Reproduced with permission [39]. Copyright 2019, American Chemical Society. **d** Photocatalytic H_2 evolution rate of pristine $MAPbI_3$ and $MAPbI_3$/CoP hybrid, **e** schematic illustration of H_2 generation process, and **f** stability test over $MAPbI_3$/CoP hybrid in $MAPbI_3$-saturated HI solution. Reproduced with permission [78]. Copyright 2020, Wiley–VCH

type-II heterogeneous photocatalyst $Cs_3Bi_2Br_9/g\text{-}C_3N_4$ with the positive band-alignment led to an efficient charge separation [83]. Interestingly, a strategy by sharing a common metal to construct type-II heterojunction based on lead-free MHPs, $MA_3Bi_2I_9/DMA_3BiI_6$ [69], was recently successfully developed with a solvent engineering technique. An

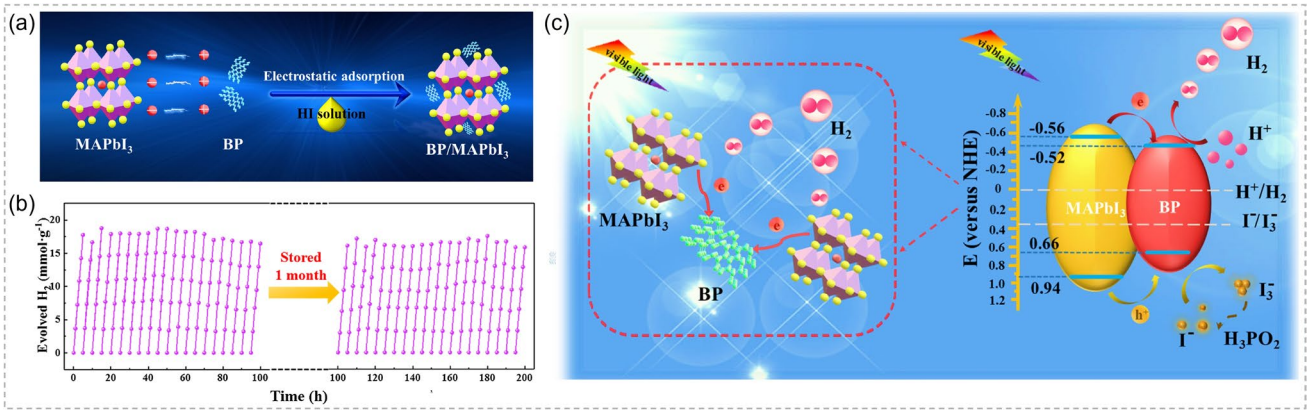

Fig. 11 **a** Schematic diagram of $BP/MAPbI_3$ preparation process, **b** cycling tests of H_2 production, and **c** photogenerated charge transfer over $BP/MAPbI_3$ under light illumination. Reproduced with permission [82]. Copyright 2019, Elsevier

enhanced photoinduced charge separation was achieved with a prolonged exciton lifetime of ~ 38 ns for the hybrid $MA_3Bi_2I_9/DMA_3BiI_6$, leading to an improvement of the solar-light-driven H_2 evolution efficiency.

3.1.4 Z-Scheme Heterojunctions for Photocatalytic H_2 Evolution

Z-scheme heterojunction has also been constructed to improve photocatalytic H_2 evolution performance of MHPs. For instance, Zeng et al. anchored two-dimensional black phosphorus (BP) onto $Cs_2AgBiBr_6$ (CABB) through electrostatic coupling [90]. The resulted Z-scheme BP/CABB showed a higher H_2 generation rate of 104.6 μmol g^{-1} h^{-1} than that of bare CABB, attributed to the key role of BP as an electronic accelerator.

3.1.5 S-Scheme Heterojunctions for Photocatalytic H_2 Evolution

Different from traditional type-II heterojunction, S-scheme heterojunction has been proved to maintain the strong redox potential. Zhang et al. constructed an S-scheme heterojunction of $Cs_2AgBiBr_6$ regular octahedron crystals with enriched Br-vacancies and WO_3 nanorods (V_{Br}-$Cs_2AgBiBr_6/WO_3$) (Fig. 12d) [86]. Owing to the fast electron transfer from WO_3 to V_{Br}-$Cs_2AgBiBr_6$, an increased and decreased electron density was observed on the surface of V_{Br}-$Cs_2AgBiBr_6$, and WO_3, respectively, indicating the formation of S-scheme heterojunction between WO_3 and V_{Br}-$Cs_2AgBiBr_6$. EPR tests indicated the generation of superoxide radical ($\cdot O_2^-$) in V_{Br}-$Cs_2AgBiBr_6/WO_3$, attributed to the reduced O_2. The presence of ·OH signal demonstrated that V_{Br}-$Cs_2AgBiBr_6/WO_3$ could oxidize H_2O/OH^- to ·OH (Fig. 12e). All these results proved the formation of S-scheme heterojunction instead of type-II heterojunction (Fig. 12f). The optimal V_{Br}-$Cs_2AgBiBr_6/WO_3$ exhibited almost 4.9-fold higher photocatalytic H_2 evolution activity than that of bare V_{Br}-$Cs_2AgBiBr_6$ (Fig. 12g).

3.2 MHPs-Based Heterojunctions for Photocatalytic CO_2 Reduction

Photocatalytic CO_2 reduction under ambient temperature to produce solar fuels or chemicals stands out as a dual-functional reaction in mitigating climate and energy crisis [91, 92]. In this process, CO_2 molecules are first adsorbed and activated and then converted into various intermediate species through sequential hydrogenation and dehydration procedure [93, 94]. Multiple photogenerated electrons are involved in this process, generating various valuable products, such as CO, CH_4, HCOOH, CH_3OH, C_2H_5OH. The detailed steps and corresponding redox potentials are shown in Eqs. 1–5 [95, 96], which are all satisfied by the CB potential of MHPs. Since the first work reported by Sun's group in 2017 [97], continuous efforts have been devoted (Table 2). In general, solar light absorption and charge-carrier separation and transport are two main factors in photocatalytic CO_2 reduction systems. The design of MHPs-based

 https://doi.org/10.1007/s40820-025-01886-y

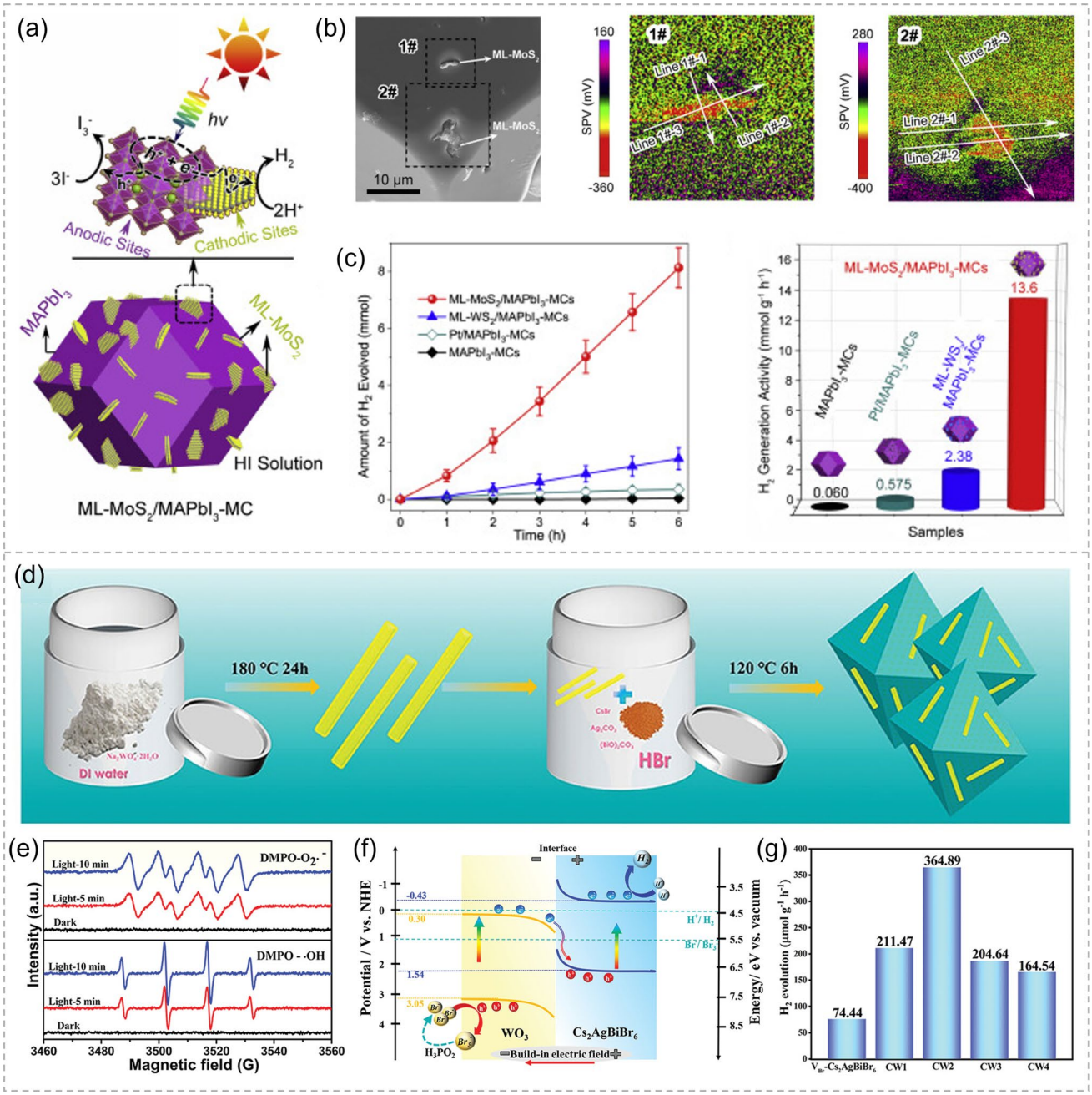

Fig. 12 **a** Schematic illustration of structural configuration and redox processes, **b** SPV distribution of ML-MoS_2/$MAPbI_3$-MCs, and **c** photocatalytic HI splitting performance over ML-MoS_2/$MAPbI_3$-MCs, ML-WS_2/$MAPbI_3$-MCs, Pt/$MAPbI_3$-MCs, and the pristine $MAPbI_3$-MCs. Reproduced with permission [84]. Copyright 2020, Elsevier. **d** Schematic illustration of V_{Br}-$Cs_2AgBiBr_6$/WO_3 fabrication process, **e** EPR spectra of DMPO- $\cdot O_2^-$ and DMPO-$\cdot$OH before and after light irradiation, and **f** schematic mechanism of the charge transfer and dynamic equilibrium processes over V_{Br}-$Cs_2AgBiBr_6$/WO_3 composite, and **g** H_2 production rate of V_{Br}-$Cs_2AgBiBr_6$/WO_3, and CW_x in aqueous HBr/H_3PO_2 solutions. Reproduced with permission [86]. Copyright 2023, Wiley–VCH

heterojunctions is one of the most popular strategies to improve efficiency over these two factors.

$$CO_2 + 2e^- + 2H^+ = CO + H_2O \ E_1 = -0.53V \ vs \ NHE \ (pH = 7) \quad (1)$$

$$CO_2 + 2e^- + 2H^+ = HCOOH \ E_2 = -0.61V \ vs \ NHE \ (pH = 7) \quad (2)$$

$$CO_2 + 4e^- + 4H^+ = HCHO + H_2O \ E_3 = -0.48V \ vs \ NHE \ (pH = 7) \quad (3)$$

$$CO_2 + 6e^- + 6H^+ = CH_3OH + H_2O \; E_4 = -0.38V \; vs \; NHE \; (pH = 7) \quad (4)$$

$$CO_2 + 8e^- + 8H^+ = CH_4 + 2H_2O \; E_5 = -0.24V \; vs \; NHE \; (pH = 7) \quad (5)$$

3.2.1 Schottky Junctions for Photocatalytic CO_2 Reduction

Metals are usually hybridized with MHPs to construct Schottky junction for CO_2 reduction. For example, a novel zero-dimensional $CsPbBr_3$ nanocrystal/two-dimensional palladium nanosheet ($CsPbBr_3$ NC/Pd NS) composite was reported to realize CO_2 reduction in H_2O vapor (Fig. 13a-c) [99]. The Schottky contact at the interface extracted the photoinduced electrons from $CsPbBr_3$ to Pd effectively, facilitating electrons injection into the subsequent chemical reactions. Su et al. encapsulated $CsPbBr_3$ and Au particles by Al-based mesoporous metal–organic framework (MOF) to prepare a ternary $CsPbBr_3$/Au/PCN-333(Al) hybrid composite [117]. The synergetic effect enabled by the Schottky contact between $CsPbBr_3$ and Au in MOF matrix improved the photocatalytic CO_2 reduction performance largely with the $R_{electron}$ exhibiting 11.5-fold enhancement compared to single $CsPbBr_3$ NCs. Moreover, the integrated PCN-333(Al) as a protective layer was used to encapsulate MHPs, leading to a good stability of the photocatalytic activity after 5 cycles.

2D MXene nanosheets (e.g., $Ti_3C_2T_x$) have recently been widely used to construct Schottky heterojunctions with MHPs for CO_2 reduction. Xing et al. presented a self-assembled heterojunction of lead-free double perovskite onto the surface of MXene ($Cs_2AgBiBr_6/Ti_3C_2T_x$) via electrostatic attraction [36]. The presence of MXene not only accelerated the formation of free charge carriers, but also enabled the ultrafast photoelectrons transfer from $Cs_2AgBiBr_6$ to MXene within 1.1 ps and prolongs the charge-carrier lifetime. Following this work, various Schottky junction heterojunctions, such as $CsPbBr_3$/$Ti_3C_2T_x$ [118], $FAPbBr_3$ QDs/Ti_3C_2 [102], $CsPbBr_3$ QDs/Ti_3C_2 [101], for enhanced photocatalytic CO_2 reduction were developed.

In addition, a composite of $CsPbBr_3$ quantum dot/graphene oxide ($CsPbBr_3$ QDs/GO) was obtained through in situ growth with the addition of GO into $CsPbBr_3$ precursor [97]. Because of the improved electron extraction and transfer, CO_2 reduction reached a rate of 23.7 μmol g^{-1} h^{-1} with an increased 25.5% electron consumption. Other carbon materials such as rGO [119], multiwalled carbon [100], C_{60} [120], nanoporous carbon power [121], etc., were also incorporated with MHPs to improve CO_2 conversion performances.

3.2.2 Type-I Heterojunctions for Photocatalytic CO_2 Reduction

Zhu and coworkers reported the first MHPs-based type-I heterojunction $CsPbBr_3$/BP for photocatalytic CO_2 reduction [42]. Pb-P interaction in $CsPbBr_3$/BP composite, revealed by the high-resolution XPS spectra, promoted the efficient transport of photogenerated electrons between excited $CsPbBr_3$ and BP. 4.4- and 2.4-fold enhancements were achieved for CO_2 photoreduction to CO and CH_4, respectively, compared to single $CsPbBr_3$. As a new member of the 2D material family, graphdiyne (GDY) was coated onto the surface of $CsPbBr_3$ nanocrystals (Fig. 13d) [67]. Under the protection of GDY, the stability of MHPs-based composites in photocatalytic system was improved. The *sp*-hybridized carbon atoms and triangular cavities in the GDY accelerated the metal atom doping to act as the active sites for photocatalytic reaction (Fig. 13e). The favorable energy alignment and close contact triggered photoelectrons transfer from $CsPbBr_3$ to active sites in GDY (Fig. 13f).

3.2.3 Type-II Heterojunctions for Photocatalytic CO_2 Reduction

Type-II heterojunction with efficient spatial separation of charge carriers has been constructed to enhance the performance of CO_2 reduction. Transition-metal oxides, chalcogenides, and sulfide, such as Co_3O_4 [122], TiO_x [123], ZnO [124], CdSe [125], etc., have shown great promise to form type-II heterojunction with MHPs. For instance, $CsPbBr_3$ NCs loaded on a hierarchical branched ZnO nanowire/microporous graphene scaffold were reported [124], achieving a boosted photocatalytic performance with a photoelectron consumption rate of 52.02 μmol g^{-1} h^{-1}. Gong et al. synthesized a zero-dimensional $CsPbBr_3$/CdSe heterojunction through a thermal injection method [125]. DFT calculations indicated that the strong interactions of

https://doi.org/10.1007/s40820-025-01886-y

Table 2 A summary of the photocatalytic activity of the MHPs-based heterojunctions toward CO_2 reduction

Photocatalysts	Hetero-junction	Reaction solution	Electron donor	Light Source	Products	Activity	Refs.
$CsCuCl_3$/Cu	Schottky junction	Ethyl acetate	Isopropyl alcohol	simulated sunlight	CH_4	21.61 μmol g^{-1}	[98]
$CsPbBr_3$ QDs/ GO	Schottky junction	Ethyl acetate	Ethyl acetate	AM 1.5G	CH_4	29.6 μmol g^{-1}	[97]
					CO	58.7 μmol g^{-1}	
$CsPbBr_3$/Bi	Schottky junction	None	Water	300 W Xe lamp	CO	76.4 μmol g^{-1}	[58]
$CsPbBr_3$ NC/Pd NS	Schottky junction	None	Water	300 W Xe lamp, > 420 nm	CH_4	3.94 μmol g^{-1}	[99]
					CO	12.63 μmol g^{-1}	
$CsPbBr_3$/ MWCNT	Schottky junction	Acetonitrile	Water	300 W Xe lamp, > 420 nm	CH_4	33.5 μmol g^{-1}	[100]
					CO	98.3 μmol g^{-1}	
$CsPbBr_3/Ti_3C_2T_x$	Schottky junction	Ethyl acetate	Ethyl acetate	300 W Xe lamp, > 420 nm	CH_4	33.83 μmol g^{-1}	[101]
					CO	133.05 μmol g^{-1}	
$FAPbBr_3/Ti_3C_2$	Schottky junction	Water	Water	Simulated sunlight	CH_4	17.67 μmol g^{-1} h^{-1}	[102]
					CO	283.41 μmol g^{-1} h^{-1}	
$CsPbBr_3$/BP	Type-I	Ethyl acetate	Water	Simulated sunlight	CH_4	32 μmol g^{-1}	[42]
					CO	134 μmol g^{-1}	
$CsPbBr_3$@GDY-Co	Type-I	Acetonitrile	Water	300 W Xe lamp, > 400 nm	CO	27.7 μmol g^{-1} h^{-1}	[67]
$CsPbBr_3/MoS_2$	Type-II	Ethyl acetate	Water	300 W Xe lamp, > 420 nm	CH_4	54.7 μmol g^{-1}	[103]
					CO	74.9 μmol g^{-1}	
Cs_2SnI_6/SnS_2	Type-II	H_2O/CH_3OH	CH_3OH	300 W Xe lamp, > 400 nm	CH_4	6.09 μmol g^{-1}	[21]
$CsSnCl_3$/ZnSe	Type-II	Toluene/ isopropanol	Isopropanol	300 W Xe lamp, > 400 nm	CO	55 μmol g^{-1} h^{-1}	[16]
$CsPbBr_3$-CdZnS	Type-II	None	Water	300 W Xe lamp	CO	55.8 μmol g^{-1} h^{-1}	[62]
$CsPbBr_3$-P3HT	Type-II	Acetonitrile	Water	300 W Xe lamp, > 420 nm	CO	145.45 μmol g^{-1} h^{-1}	[55]
					CH_4	23.05 μmol g^{-1} h^{-1}	
$Cs_2AgBiBr_6$/ Ce-UiO-66-H	Type-II	None	Water	300 W Xe lamp	CO	309.01 μmol g^{-1} h^{-1}	[104]
g-C_3N_4@ $Cs_2AgBiBr_6$	Type-II	Ethyl acetate/ water	Triethylamine	300 W Xe lamp, > 420 nm	CO	35.52 μmol g^{-1}	[105]
					CH_4	3.91 μmol g^{-1}	
g-C_3N_4-$CsPbBr_3$	Type-II	Acetonitrile	Water	300 W Xe lamp, > 420 nm	CO	149 μmol g^{-1}	[106]
α-Fe_2O_3/Amine RGO/$CsPbBr_3$	Z-scheme	None	Water	300 W Xe lamp, > 420 nm	CH_4	9.45 μmol g^{-1} h^{-1}	[107]
LF-$FAPbBr_3$/α-Fe_2O_3	Z-scheme	None	Water	300 W Xe lamp, > 400 nm	CO	45.5 μmol g^{-1} h^{-1}	[108]
					CH_4	10.5 μmol g^{-1} h^{-1}	
$SnS_2/CsPbBr_3$	Z-scheme	None	Water	300 W Xe lamp, 300–800 nm	CO	1.98 μmol g^{-1} h^{-1}	[109]
$CsPbBr_3$/ $CsPb_2Br_5$	Z-scheme	None	Water	300 W Xe lamp	CO	197.11 μmol g^{-1} h^{-1}	[70]
$CsPbBr_3$/NiFe-LDH	Z-scheme	Ethyl acetate/ isopropanol	Isopropanol	300 W Xe lamp, > 420 nm	CO	10.5 μmol g^{-1} h^{-1}	[110]
					CH_4	2.64 μmol g^{-1} h^{-1}	
PCN-222/ $CsPbBr_3$	Z-scheme	Acetonitrile	Triethylamine	300 W Xe lamp, > 420 nm	HCOOH	189.9 μmol g^{-1} h^{-1}	[111]
$Cs_3Bi_2I_9/Bi_2WO_6$	Z-scheme	None	Water	300 W Xe lamp, > 400 nm	CO	66 μmol g^{-1}	[112]
Ni-doped $CsPbBr_3$/ Bi_3O_4Br	Z-scheme	None	Water	300 W Xe lamp	CO	387.57 μmol g^{-1} h^{-1}	[113]
$BiVO_4/CsPbBr_3$	S-scheme	None	Water	300 W Xe lamp	CO	68 μmol g^{-1}	[53]
$CsPbBr_3$/BiOCl	S-scheme	Ethyl acetate	Water	300 W Xe lamp	CO	34.72 μmol g^{-1} h^{-1}	[60]
					CH_4	3.47 μmol g^{-1} h^{-1}	
$Cs_3Bi_2Br_9$/Bi-MOF	S-scheme	None	Water	300 W Xe lamp	CO	572.24 μmol g^{-1} h^{-1}	[114]

Table 2 (continued)

Photocatalysts	Hetero-junction	Reaction solution	Electron donor	Light Source	Products	Activity	Refs.
$Cs_3Bi_2Br_9$@M-Ti framework	S-scheme	Isopropanol	Isopropanol	300 W Xe lamp, 200–1100 nm	CH_4	32.9 μmol g^{-1} h^{-1}	[115]
$SnO_2/Cs_3Bi_2Br_9$	S-scheme	Acetonitrile	Water	300 W Xe lamp	CH_4	21.4 μmol g^{-1}	[116]

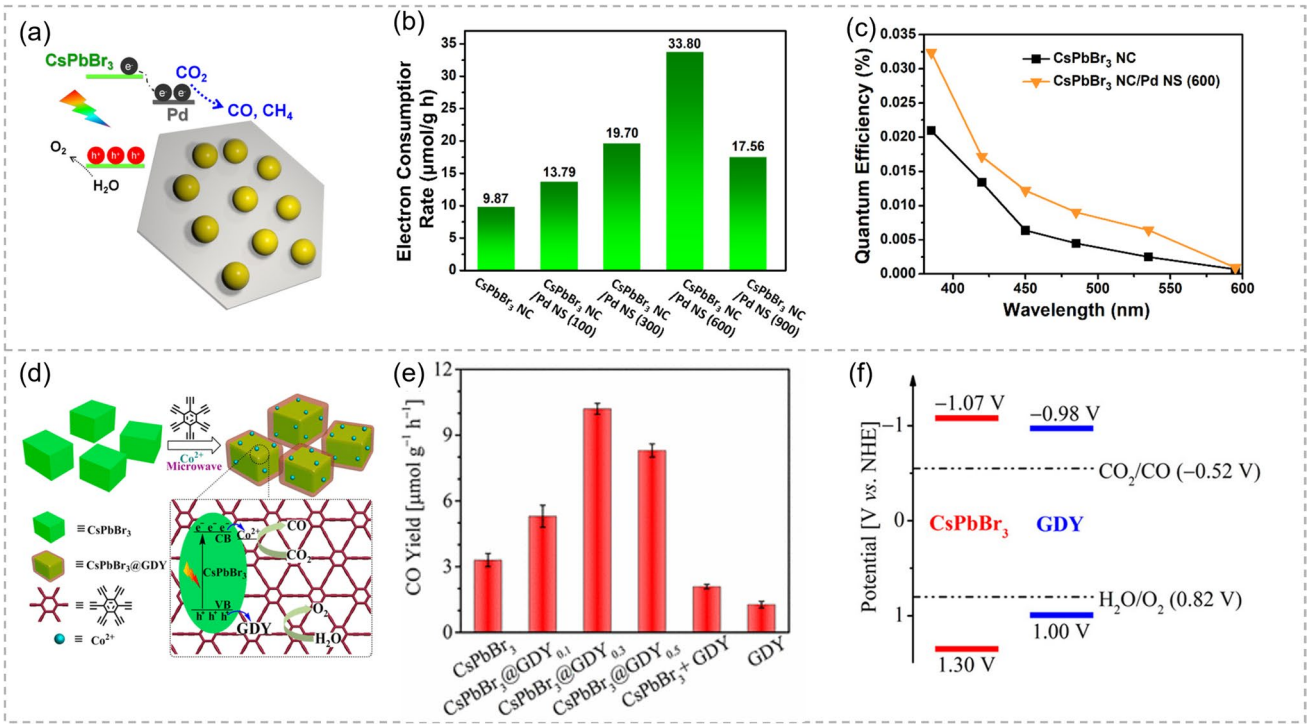

Fig. 13 **a** Mechanism of $CsPbBr_3$/Pd photocatalytic CO2 reduction, **b** the rate of electron consumption, and **c** the quantum efficiency of the hybrid under different wavelength. Reproduced with permission [99]. Copyright 2018, American Chemical Society. **d** Illustration of the cobalt-doped $CsPbBr_3$@GDY preparation process, **e** CO production yield of CO_2 photoreduction with $CsPbBr_3$, $CsPbBr_3$@$GDY_{0.1–0.5}$, a mixture of $CsPbBr_3$ and GDY, and GDY as photocatalysts, and **f** energy band alignment of $CsPbBr_3$ and GDY. Reproduced with permission [67]. Copyright 2020, American Chemical Society

Pb-Se and Br-Cd chemical bonding in the type-II heterojunction effectively facilitated electron transfer. Cs_2SnI_6 perovskite nanocrystal/SnS_2 nanosheet heterojunctions with an atomic-level close-contact interface prolonged the lifetime of photogenerated electrons in SnS_2 from 1290 to 3080 ps [21]. Other type-II heterojunctions such as $CsSnCl_3$/ZnSe [16] and $CsPbBr_3/MoS_2$ [103] were also reported for photocatalytic CO_2 reduction.

Besides, metal-free organic materials have been investigated to construct type-II heterojunctions. For example, Xu et al. encapsulated $CsPbBr_3$ QDs into a poly(3-hexylthiophene-2,5-diyl) (P3HT) protective layer to fabricate an efficient P3HT/$CsPbBr_3$ type-II heterojunction [55]. The introduced P3HT with high carrier mobility could transport the carriers to surface quickly and act as an electron donor to donate photogenerated electrons to MHPs for CO_2 reduction to CO and CH_4. CTFs (covalent triazine frameworks) were coupled with $CsPbBr_3$ QDs via an electrostatic self-assembly approach (Fig. 14a, b) [61]. The synergistic interactions between $CsPbBr_3$ and CTF, as well as effective visible light harvesting and abundant catalytic sites, led to excellent photocatalytic activity toward CO_2 reduction with an AQE of 0.07% at 450 nm. The protective effect of CTFs onto $CsPbBr_3$ QDs enabled stable photocatalytic activity. Porous g-C_3N_4 with abundant amino sites on the edges were coupled with $CsPbBr_3$ QDs

 https://doi.org/10.1007/s40820-025-01886-y

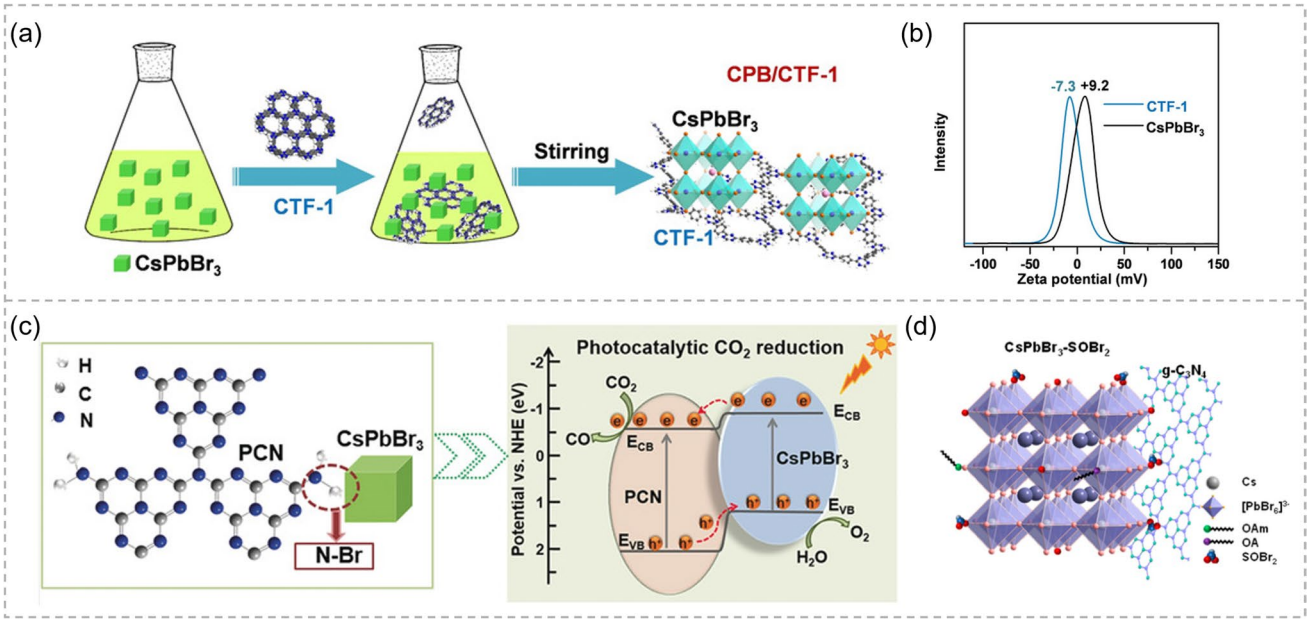

Fig. 14 **a** Schematic illustration for the formation of the CPB/CTF-1 and **b** ξ potentials of the pristine CTF-1 and $CsPbBr_3$ QDs. Reproduced with permission [61]. Copyright 2021, Wiley–VCH. **c** Illustrations of constructed CPB-PCN via N-Br bond and band alignment of the composite. Reproduced with permission [106]. Copyright 2018, Wiley–VCH. **d** Schematic illustration of the photocatalytic mechanisms of the $CsPbBr_3$-$SOBr_2$/g-C_3N_4. Reproduced with permission [126]. Copyright 2022, American Chemistry Society

(Fig. 14c) with the formation of N-Br bonding [106]. DFT calculations suggested the unique N-Br bonding promoted the charge carriers' dynamics, thus leading to 15 times higher activity for CO_2 reduction to CO compared to pure QDs. The robust connection was also established between $CsPbBr_3$ medicated with $SOBr_2$ and g-C_3N_4 (Fig. 14d) [126].

3.2.4 Z-Scheme Heterojunctions for Photocatalytic CO_2 Reduction

The mostly reported materials for MHPs-based Z-scheme heterojunctions were transition-metal oxides [72, 107, 108, 127, 128] and sulfide [109]. An all-solid-state Z-scheme system was fabricated with $CsPbBr_3$ and α-Fe_2O_3 using ultrathin and small-size graphene oxide (USGO) nanosheets as the electron mediator [72]. $CsPbBr_3$ and α-Fe_2O_3 can be closely anchored onto USGO nanosheets through chemical bonds with abundant function groups on USGO surface (Fig. 15a), i.e., carboxyl, hydroxyl, thus facilitating charge separation and transfer (Fig. 15b, c) [107]. A high electron consumption rate of 147.6 μmol g^{-1} h^{-1} for CO_2-to-CO conversion was achieved. SnS_2 without catalytic activity toward CO_2 reduction was deposited on $CsPbBr_3$ NCs to form SnS_2/$CsPbBr_3$ Z-scheme heterojunction, and 2.4-fold higher activity of CO was obtained (Fig. 15d) [109]. Inorganic oxide perovskite with the formula of ABO_3 (where A is an alkaline-earth metal; B is transition metal) was also developed. Li et al. reported one example of direct Z-scheme heterostructure $Cs_2AgBiBr_6$/Sr_2FeNbO_6 (CABB/SFNO) double perovskites [129]. The different work functions and Fermi levels enabled the electron transfer from the CB of SFNO to VB of CABB under light irradiation, illustrating a direct Z-scheme electron transfer mode. Fu et al. have fabricated a Cu-BTC-encapsulated $CsPbBr_3$ QDs core/shell Z-scheme heterojunction. The existing coating layer improved the stability in moisture remarkably [130].

Metal-free carbon nitride materials were also introduced to fabricate Z-scheme heterojunction for CO_2 reduction. $Cs_2AgBiBr_6$@g-C_3N_4 Z-scheme was constructed by regulating the used solvent during in situ assembly process [49]. By combining the reduction ability of CB of g-C_3N_4 and oxidization ability of VB of $Cs_2AgBiBr_6$, Z-scheme system showed a high CH_4 selectivity in CO_2 photoreduction. P-modified g-C_3N_4 was further incorporated to fabricate P-CN/$CsPbBr_3$ [131]. Because the CB position is not

negative enough to reduce CO_2 to CO, the Z-scheme mechanism was considered to be formed instead of type-II. The P-CN/$CsPbBr_3$ obtained a superior CO_2 reduction to CO with the yield enhancement of 7.2- and 1.2-fold compared to pristine P-CN and $CsPbBr_3$, respectively.

3.2.5 S-Scheme Heterojunctions for Photocatalytic CO_2 Reduction

Yu et al. reported the first work about metal oxide/MHPs (TiO_2/$CsPbBr_3$) S-scheme heterojunction for photocatalytic CO_2 reduction [132]. DFT calculations revealed that the internal electric field promoted the transfer of photogenerated electrons in CB of TiO_2 to VB of $CsPbBr_3$. An et al. modulated the exposed facets of TiO_2 in S-scheme heterojunction to simultaneously optimize the interfacial and surface electronic structures for directional charge migration [133]. Other metal oxides including WO_3 [134, 135], ZnO [136], SnO_2 [116, 137], and Cu_2O [138] were also studied to construct S-scheme heterojunctions. Lu et al. deposited lead-free $Cs_3Sb_2Br_9$ nanocrystals onto the surface of Co_3O_4 to generate a S-scheme heterojunction via polymer-assisted growth method. Due to the enhanced charge separation efficiency, the composites showed excellent activity of CO_2 reduction to CO with the yield of 700.7 μmol g^{-1} h^{-1} [139].

Bismuth-based materials with highly anisotropic Fermi surface, small electron effective mass and band gap, and large electron meant free path have attracted great interests to construct S-scheme heterojunctions [140–142]. A bismuthine/$CsPbBr_3$ QDs S-scheme heterojunction was prepared through in situ growth [143]. The introduction of narrow band gap bismuthine enhanced light absorption abilities and suppressed the recombination of charge carriers. BiOCl with a band gap of 3.2–3.6 eV was used to fabricate 2D/2D $CsPbBr_3$/BiOCl S-scheme photocatalyst, and a much enhanced CO_2 photoreduction performance was obtained [60]. Other Bi-based materials, such as 2D Bi_2WO_6 (BWO) [144, 145], Bi-MOF [114], and $BiVO_4$ [53], were also reported. In addition, lead-free $Cs_2AgBiBr_6$/$BiVO_4$ S-scheme heterojunction was prepared through electrostatic assembly. Under the optimal conditions, the composite showed 9.2-time enhancement compared to $Cs_2AgBiBr_6$ alone. DFT calculations revealed that the main active sites for CO_2 photocatalytic reduction were Ag sites [146].

Except for metal materials, g-C_3N_4 was designed to encapsulate $CsPbBr_3$ nanoparticles to obtain a water-stable core/shell S-scheme heterojunction (m-CN@$CsPbBr_3$)

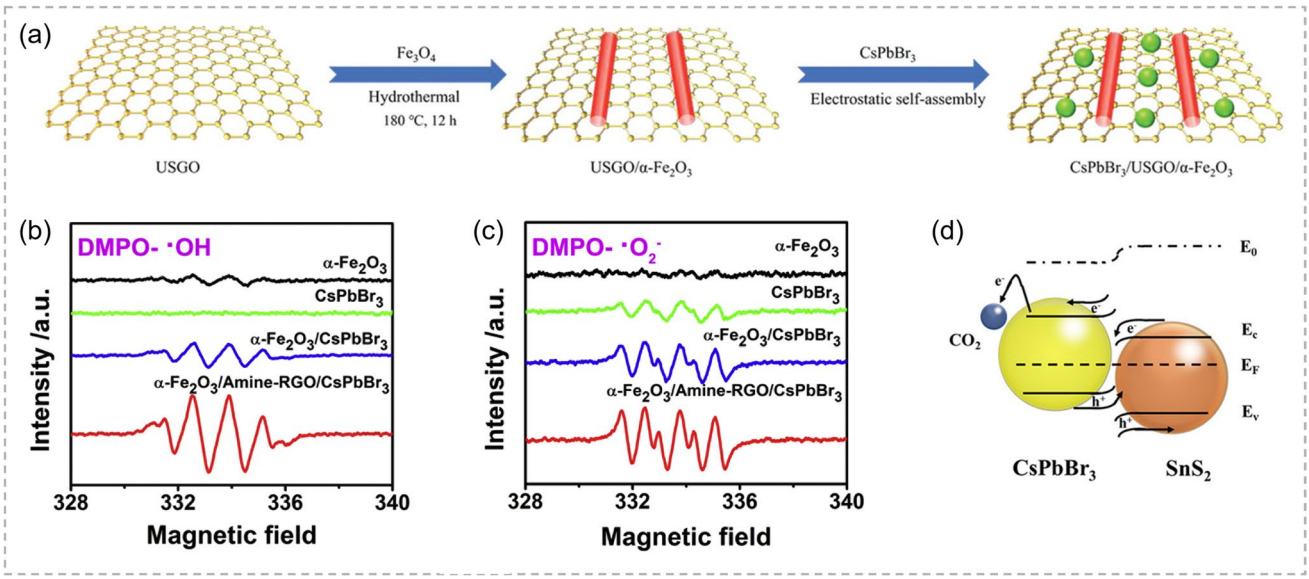

Fig. 15 **a** Schematic illustrations of $CsPbBr_3$/USGO/α-Fe_2O_3 synthesis processes. Reproduced with permission [72]. Copyright 2020, Wiley–VCH. EPR spectra of **b** DMPO-•OH in water/methyl cyanide and **c** DMPO-$\cdot O_2^-$ in O_2/methylcyanide in the presence of α-Fe_2O_3, $CsPbBr_3$, α-Fe_2O_3/$CsPbBr_3$, and α-Fe_2O_3/amine-RGO/$CsPbBr_3$. Reproduced with permission [107]. Copyright 2020, Elsevier. **d** Mechanism of charge-carrier transfer process of CO_2 reduction based on SnS_2/$CsPbBr_3$ NC heterojunction. Reproduced with permission [109]. Copyright 2022, Wiley–VCH

https://doi.org/10.1007/s40820-025-01886-y

[147]. The rich adsorption and activation sites of CO_2 molecules as well as polar surface resulted in an outstanding activity of CO_2-to-CO with the yield of 42.8 μmol g^{-1} h^{-1}. S-doped g-C_3N_4 was further used to construct S-g-C_3N_4/$CsPbBr_3$ S-scheme heterojunction, which not only improved the charge separation, but also enhanced the visible-light response.

3.2.6 Hybrid Heterojunctions for Photocatalytic CO_2 Reduction

Besides the above single heterojunctions, hybrid heterojunctions, consisting of two or more heterojunctions, have also been constructed. For example, Lu et al. have developed a ternary MHPs-based heterojunction, TiO_2/MHP/GDY, in which a Z-scheme and a typical type-I heterojunction were formed, through a self-templating method combined with sequential deposition technology [148]. Because of the unique sandwich structure, the photocatalysts possessed an exceptional stability in water-containing environments for durations exceeding 200 h. Hou et al. reported a novel composite photocatalyst system for artificial photosynthesis through embedding MHPs in functionalized MOF glass, in which a type-I and type-II heterojunction interfaces were simultaneously formed. Photoinduced electrons were efficiently generated under light irradiation and transferred for coenzyme regeneration, which could then be consumed by immobilized enzymes for CO_2 reduction to formic acid [149].

3.3 MHPs-Based Heterojunctions for Photocatalytic Organic Pollutant Degradation

With the rapid industrialization and urbanization, water pollution has become a global issue. The most representative pollutants are toxic organic dyes, such as rhodamine B (RhB), 4-nitrophenol (4-NP), and methylene blue (MB). Photocatalytic technology is an efficient and cost-effective way to degrade the pollutant into low toxicity inorganic small molecules. For photo-degradation organic pollutants, photo-induced electrons in CB of semiconductors firstly reduce O_2 to generate superoxide radicals $^{\bullet}O_2^-$ and then react with target pollutants. The degradation efficiency is denoted as C/C_0, where C_0 and C represent the absorption intensity of dye before and after illumination. Most MHPs possess high CB levels, which are feasible enough to produce reactive oxygen species. Several results about MHPs degrading organic dyes have been reported, especially MHPs-based heterojunctions [150].

3.3.1 Schottky Junctions for Photocatalytic Organic Pollutant Degradation

In 2019, Huang et al. deposited Au nanoparticles on $CsPb(Br_{1-x}Cl_x)_3$ to degrade Sudan Red III under visible light irradiation (Fig. 16a) [151]. The composite achieved 71% of Sudan Red III degradation within 6 h (Fig. 16b, c). To avoid the pollution from MHPs, $Cs_2AgBiBr_6$ was employed to fabricate Pt/$Cs_2AgBiBr_6$ for degradation [152], in which four different dyes including Rhodamine B (RhB), Rhodamine 110 (Rh110), Methyl red (MR), and Methyl orange (MO) were involved in the investigation. In addition, γ-$CsPbI_3$ NCs/WS_2 Schottky junction was also reported to degrade Methylene blue [35]. The superior carrier-transport property of few-layered WS_2 nanosheets enabled a high photocatalytic degradation efficiency of nearly 100% in 30 min.

3.3.2 Type-I Heterojunctions for Photocatalytic Organic Pollutant Degradation

Liu et al. reported one type-I heterostructure example of Ag-$CsPbBr_3$/CN toward 7-aminocephalosporanic acid (7-ACA) degradation [153]. A superior photocatalytic activity was achieved with degradation efficiency of 92.79% toward 7-ACA within 140 min. Experiment results revealed that the improved photocatalytic activity was attributed to the excellent adsorption capacity, enhanced light harvesting, and reduced charge recombination. Photoinduced holes and hydroxyl radicals played major roles, which could attack 7-ACA molecules to degrade into CO_2, H_2O and other small molecules, while electrons and superoxide radical played minor roles based on relative reactive-species-trapping experiments.

3.3.3 Type-II Heterojunctions for Photocatalytic Organic Pollutant Degradation

Owing to the facilitated charge-carrier dynamics, Chattopadhyay et al. embraced polymeric graphitic carbon nitride

($g\text{-}C_3N_4$) and all-inorganic cesium lead halide perovskite ($CsPbBrCl_2$) to construct type-II heterojunction [154]. The generation of active radicals resulted in much improved performance in cationic and anionic dyes degradation. In addition, poly(norepinephrine) (PNE) was used to encapsulate MHPs to improve chemical stability. The existing hydroxyl group in the side chain results in a well-controlled, ultrasmooth coating layer and reduced aggregation during polymerization. $MAPbBr_3$ (M-PE) NPs were covered with PNE layer via a surface growth method [155]. Benefitting from the coating layer of PNE, the obtained M-PE@PNE core@shell not only showed great stability but also exhibited excellent malachite green degradation efficiency (81% in less than 2 h), almost 8-time enhancement compared with pristine M-PE NPs (Fig. 16d-f). Abdukayum et al. reported a lead-free MHPs-based heterojunction photocatalyst of $Cs_2AgBiI_6/g\text{-}C_3N_4$ for RhB degradation, outperforming Cs_2AgBiI_6 by a factor of 1.3. The improved photocatalytic performance was attributed to the improved charge

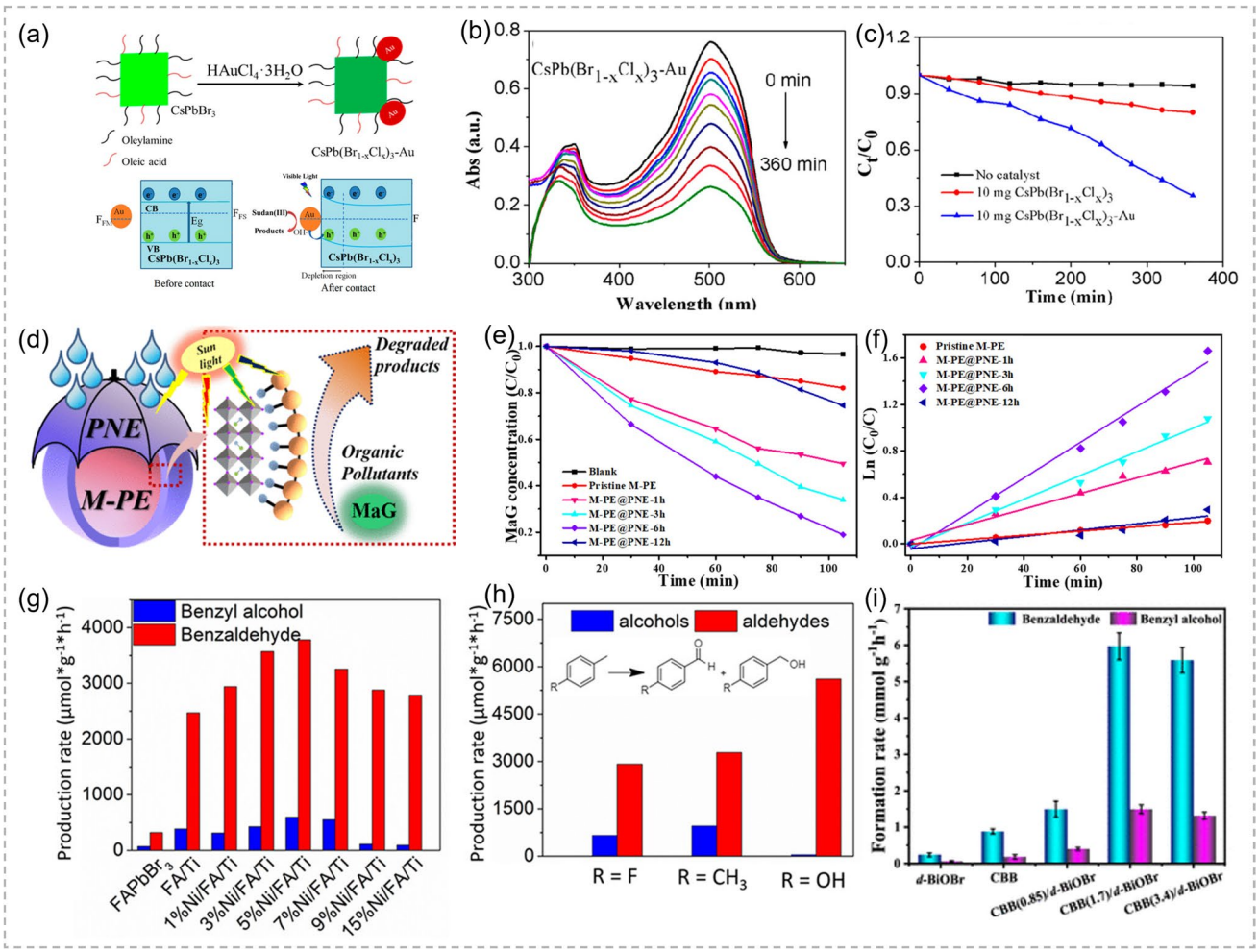

Fig. 16 **a** Reduction of Au(III) at the surface of $CsPbBr_3$ NCs to form $CsPb(Br_{1-x}Cl_x)_3$-Au heterojunctions and proposed photocatalytic mechanisms, **b** absorption spectra of Sudan Red III degraded using $CsPb(Br_{1-x}Cl_x)_3$-Au heterojunctions, and **c** concentration (C_t/C_0) changes *vs* time of Sudan Red III using different catalysts. Reproduced with permission [151]. Copyright 2019, American Chemistry Society. **d** Schematic illustration of M-PE@PNE photodegradation organic pollutants, **e** plots of C/C_0 *vs* time for the photocatalytic degradation of MaG (3.0 mg L^{-1}) in the presence of pristine M-PE and MPE@PNE-1/3/6/12 h under visible light, and **f** plots of $\ln(C_0/C)$ *vs* irradiation time with the fitting results included. Reproduced with permission [155]. Copyright 2020, American Chemistry Society. Photocatalytic oxidation of $C(sp^3)$-H in **g** Tol and **h** substituted toluene over $NiO_x/FAPbBr_3/TiO_2$. Reproduced with permission [157]. Copyright 2019, American Chemistry Society. **i** Comparison of photocatalytic toluene oxidation over d-BiOBr, CBB, and the CBB/d-BiOBr composite. Reproduced with permission [158]. Copyright 2022, American Chemistry Society

 https://doi.org/10.1007/s40820-025-01886-y

separation and transfer across the heterojunction interface owing to the band alignment effects [156].

3.3.4 Z-Scheme Heterojunctions for Photocatalytic Organic Pollutant Degradation

In 2018, Zeng et al. prepared Z-scheme $MASnI_3/TiO_2$ heterojunctions via a hydrothermal method [159]. The calcined $MASnI_3/TiO_2$ (1:6) enabled RhB concentration decreased to 1% within 50 min of light irradiation. $Cs_3Bi_2I_9$/g-C_3N_4 constructed based on nitrogen–iodine chemical bonding was also reported as a new binary photocatalyst for degradation of RhB, MB, MO and the mixture of MB and MO [160]. A ternary Z-scheme Ag/$CsPbBr_3/Bi_2WO_6$ photocatalyst was reported by Xu et al., in which Ag nanoparticles were used as charge mediators in heterojunction [161].

3.3.5 S-Scheme Heterojunctions for Photocatalytic Organic Pollutant Degradation

S-scheme $CsPbBr_3$-rGO/Bi_2WO_6 heterojunction was synthesized via electrostatic adsorption by forming -COO-Bi-O- bond, in which mercaptopropionic acid (MPA) was capped onto $CsPbBr_3$ surface [162]. The concentrations of norfloxacin were tested by time-dependent UV spectrum and time-dependent HPLC spectrum. The results revealed that the degradation rate was about 66.79% with 120 min under visible light irradiation. The excellent performance was owing to expanding light-harvesting scope, enhanced charge-carrier transport property, and exposed active species.

3.4 MHPs-Based Heterojunctions for Photocatalytic Organic Synthesis

Value-added chemicals, pharmaceuticals, and preservatives synthesized by organic transformation from raw materials via heterogeneous photocatalytic technique have attracted wide interests in recent years. According to the kinds of substrate molecules, we have classified organic synthesis reaction into C(sp^3)-H bond activation, radical addition, thiols oxidation, and alcohols oxidation.

3.4.1 MHPs-Based Heterojunctions for C(sp^3)-H Bond Activation

The activation of inert C(sp^3)-H bond is one of the most challenging reactions in organic synthesis. Traditional C(sp^3)-H bond activation is achieved by thermal catalysis with the help of noble metals under high temperature and pressure. Recently, heterogeneous photocatalysis with MHPs as photocatalysts to activate C(sp^3)-H bond using oxygen as oxidant seems to be a potential avenue.

Type-II heterojunctions for C(sp^3)-H bond activation: Li et al. fabricated a series of $CsPbBr_3/TiO_2$ type-II heterojunction photocatalysts via the ligand-assisted reprecipitation method toward aromatic C(sp^3)-H bond conversion with toluene as substrate [163]. The optimal sample exhibited a fourfold and threefold higher activity than that of bare $CsPbBr_3$ and TiO_2, respectively. In addition, TiO_2 and NiO_x as electron and hole transporting layers were introduced, respectively, to form $NiO_x/FAPbBr_3/TiO_2$ to promote charge separation and transfer, in which two type-II heterojunctions were formed [157]. An external quantum efficiency of 0.25% at 400 nm was achieved (Fig. 16g, h). To make reaction conditions greener, lead-free MHPs were involved in designing $Cs_3Bi_2Br_9$/CdS [45] and $Cs_3Bi_2Br_9$/g-C_3N_4 [164] heterojunctions for C(sp^3)-H bond activation.

Z-scheme heterojunctions for C(sp^3)-H bond activation: A Z-scheme structure modulated by interfacial chemical bonding through in situ growth of $Cs_3Bi_2Br_9$ nanodots on defective BiOBr nanosheets for toluene oxidation was constructed (Fig. 16i) [158]. Owing to the formed interfacial internal electric field, Bi-Br bond acted as a direct avenue for electron transfer, leading to a higher charge localization on the surface. In situ infrared Fourier transform spectroscopy and DFT calculations revealed that surface localization of holes was essential for toluene adsorption and the dissociation of C(sp^3)-H and identified the key intermediates and active sites. Chen et al. designed $Co_xBi_{2-x}O_2CO_3$ nanosheets and used as self-template to epitaxially grow $Cs_3Bi_2Br_9$ via Bi atom bridge [165]. The incorporated Co^{3+} played critical roles in heterojunction growth by regulating electronic structure and growth dynamics of $Cs_3Bi_2Br_9$, enabling significantly enhanced toluene photo-oxidation performances.

3.4.2 MHPs-Based Heterojunctions for Radical Addition

Recently, Ravelli et al. reported one example of MHPs-based heterojunctions for radical addition reaction. Lead-free perovskite, $Cs_2AgBiBr_6$, was selected to couple with g-C_3N_4 to construct a type-II heterojunction [166]. The improved charge-carrier dynamics enabled the atom transfer radical addition-type carbohalogenation of multiple C–C bonds, such as alkenes, alkynes, with alkyl halides.

3.4.3 MHPs-Based Heterojunctions for Thiols Oxidation

Disulfides are of interest as protecting groups in synthetic applications and as vulcanizing agents for rubber, which were usually obtained from oxidative coupling of thiols. To avoid overoxidation, various stoichiometric oxidants were used. In 2025, Le et al. reported a Schottky junction of $CsPbBr_3/Ti_3C_2T_x$ MXene for thiols oxidation. The production rate was up to 29,700 μmol g^{-1} h^{-1} in air without any additional oxidants [167].

3.4.4 MHPs-Based Heterojunctions for Alcohols Oxidation

The selective oxidation of alcohols into carbonyls is an important reaction in organic synthesis, which is usually performed by stoichiometric inorganic/organic oxidants, such as permanganate, dichromate, 2,2,6,6-tetramethylpiperidine oxide, and noble metal catalysts. To avoid these harsh conditions, photocatalytic techniques have been employed to oxide alcohol using O_2 as sole oxidant, resulting in high conversion and selectivity.

Type-II heterojunctions for alcohols oxidation: In 2018, Roeffaers et al. built a type-II heterojunction of $FAPbBr_3/TiO_2$ with antisolvent precipitation method for photocatalytic oxidation of benzyl alcohols in a polar solvent [168]. The highest photocatalytic conversion of benzyl alcohol peaked at 63%, totally a 4-time enhancement over the pure controls. Moreover, the composite $CsPbX_3/W_{18}O_{49}$ showed high selectivity toward selective oxidation of benzyl alcohol to benzaldehyde and a conversion up to 72%, which is 11, 10, and 2.5 times higher than that of pure $CsPbCl_3$, $CsPbBr_3$, and $W_{18}O_{49}$, respectively [68].

Z-scheme heterojunctions for alcohols oxidation: Zhang et al. constructed Z-scheme heterojunction $FAPbBr_3$ nanocrystals/WO_3 with an outstanding permanence of benzyl alcohol oxidation to benzaldehyde with selectivity of 99% [169]. Astonishingly, after the size of $FAPbBr_3$ reduced to quantum dots, benzoic acid was found as the main product with 90% selectivity. $FAPbBr_3/Bi_2WO_6$ was developed for benzyl alcohol oxidation to benzaldehyde coupled with CO_2 reduction to CO [63]. Ultrafast transient infrared absorption revealed photocarrier dynamics and demonstrated Z-scheme charge transfer mechanisms.

4 Conclusions and Outlook

MHPs with high molar extinction coefficient, tunable band gap, and high carrier mobilities have aroused huge interest in photocatalytic redox reactions but still suffer from some intrinsic limitations, e.g., inferior stability, severe charge-carrier recombination, and limited active sites. Construction of heterojunctions has been demonstrated to effectively overcome these shortcomings and has made great progress. This review summarized the recent progress of MHPs-based heterojunctions (e.g., Schottky junction, type-I, type-II, Z-scheme, S-scheme) for solar-light-driven redox reactions, including H_2 evolution, CO_2 reduction, organic pollutant degradation, and organic synthesis. On the one hand, the formation of heterojunctions promotes spatial separation of electrons and holes, thus significantly enhancing the photocatalytic activity. On the other hand, the addition of other materials could passivate the surface of MHPs, leading to improved stability. Although MHPs-based heterojunction photocatalysts have been widely investigated and significant achievements have been made, the research of MHPs-based heterojunctions in photocatalysis is still at the preliminary stage. Several challenging issues need to be solved in the future.

I. The stability of heterojunctions needed to be improved, especially in water/aqueous solution due to the inherent nature of ionic semiconductors. Several stabilization strategies such as encapsulation, surface passivation, or compositional engineering can be considered in the future. For example, protective matrices such as porous metal–organic frameworks (MOFs), graphene oxide, or polymers (e.g., poly(norepinephrine)) can physically shield MHPs

 https://doi.org/10.1007/s40820-025-01886-y

from environmental degradation while maintaining charge transport. Ligand engineering (e.g., halogen-rich surfaces or organic capping agents), which mitigates surface defects and ion migration, could improve the durability due to passivated interfacial traps.

II. The influence of heterointerface structure, such as interface locations, sizes, and coupling forces (chemical bonding or van der Waals' interaction) on photogenerated charge-carrier dynamics and photocatalytic performance, needs to be disclosed. A more in-depth understanding of these factors would provide guidance for researchers to construct high-performance heterojunctions.

III. Advanced characterization techniques need to be involved. Although some advanced characterizations such as EPR and KPFM are utilized, they are based on the relative location of band edge and standard redox potential of active species, which are not accurate. Therefore, in situ and operando characterizations under realistic reaction conditions to reveal the fine structures and behaviors of photogenerated charge carriers during the reaction are needed. For example, in situ KPFM characterization could give information about interfacial charge redistribution under light irradiation, clarifying the role of heterojunction interfaces in charge separation. Using in situ XPS characterization to measure the surface charge transfer to reveal whether the photogenerated electrons or holes transferred to photocatalysts surface, is important for the subsequent reactions. Femtosecond time-resolved transient absorption spectroscopy could be measured to reveal the photogenerated exciton relaxation progress, which could give evidence about the interaction between exciton and reactant molecule. Moreover, operando microscopy (e.g., TEM or SEM) coupled with environmental cells could reveal the structural evolution of photocatalysts (e.g., phase stability, defect formation) during reaction, addressing stability challenges. In situ Fourier transform infrared spectroscopy (FTIR) can identify intermediate species during CO_2 reduction or organic synthesis, linking interfacial properties to product selectivity. These techniques would bridge the gap between static characterization and real-time performance, enabling a deeper understanding of structure–activity relationships.

IV. Specific active sites need to be introduced into heterojunctions to realize target products generation. Taking CO_2 reduction reaction as an example, improving the products selectivity is significant. In the present, the products for CO_2 reduction were mainly simple products (e.g., CO, CH_4) with limited selectivity for C_2+ compounds. Introducing tailored active sites (e.g., single-atom catalysts or bimetallic cocatalysts) could steer reactions toward higher-value products like ethylene or ethanol.

V. While this review focuses on experimental advances, DFT studies have significantly contributed to understanding MHP heterojunctions. Computational works have clarified band alignment, interfacial charge transfer, and defect effects in Schottky, type-II, and S-scheme systems (e.g., $CsPbBr_3$/CdSe, $Cs_2AgBiBr_6$/WO_3). Future DFT efforts should target descriptor-based design (e.g., adsorption energies, charge localization) and multiscale modeling to bridge atomic-scale insights with macroscopic performance.

VI. The introduction of sacrificial reagents should be avoided. In most reported works, electron donors such as isopropanol, hypophosphoric acid, are involved, especially in H_2 evolution reaction. Valuable synthesis reactions should be introduced to utilize oxidation ability of photogenerated holes or generated halogen radical anion intermediate to produce useful chemicals, which seems more promising for further applications.

VII. Most reported photocatalytic organic synthesis is only a simple oxidation reaction, such as oxidation of alcohol/aldehyde/toluene, which usually involves one substrate. More complex substrates with functional groups need to be involved. Moreover, multicomponent redox reaction should be developed to generate compounds with various functional groups as frameworks of medicine, pesticide, or maquillage, etc.

The future of MHP-based heterostructures lies in interdisciplinary efforts combining advanced characterization, computational design, and innovative reactor engineering. Addressing these challenges could unlock their full potential for sustainable solar-to-chemical conversion, impacting energy, and environmental sectors globally. Collaborative research across academia and industry will be pivotal in transitioning these materials from lab-scale breakthroughs to real-world applications.

Acknowledgements This work was financially supported by National Natural Science Foundation of China (No. 22302155), the Fundamental Research Funds of the Center Universities (No. D5000240188), and the research program of ZJUT (YJY-ZS-20240001).

Author Contributions Qing Guo contributed to conceptualization and original draft writing. Jin-Dan Zhang was involved in literature review. Jian Li contributed to editing, review, and supervision. Xiyuan Feng contributed to editing, review, and supervision.

Declarations

Conflict of Interest The authors declare no interest conflict. They have no known competing financial interests or personal relationships that could have appeared to influence the work reported in this paper.

References

1. G. Jia, Y. Zhang, J.C. Yu, Z. Guo, Asymmetric atomic dual-sites for photocatalytic CO_2 reduction. Adv. Mater. **36**(38), 2403153 (2024). https://doi.org/10.1002/adma.202403153
2. B. Samanta, Á. Morales-García, F. Illas, N. Goga, J.A. Anta et al., Challenges of modeling nanostructured materials for photocatalytic water splitting. Chem. Soc. Rev. **51**(9), 3794–3818 (2022). https://doi.org/10.1039/d1cs00648g
3. Y. Shi, Z. Zhao, D. Yang, J. Tan, X. Xin et al., Engineering photocatalytic ammonia synthesis. Chem. Soc. Rev. **52**(20), 6938–6956 (2023). https://doi.org/10.1039/d2cs00797e
4. T. Takata, L. Lin, T. Hisatomi, K. Domen, Best practices for assessing performance of photocatalytic water splitting systems. Adv. Mater. **36**(44), 2406848 (2024). https://doi.org/10.1002/adma.202406848
5. X.-B. Li, Z.-K. Xin, S.-G. Xia, X.-Y. Gao, C.-H. Tung et al., Semiconductor nanocrystals for small molecule activation-*via*artificial photosynthesis. Chem. Soc. Rev. **49**(24), 9028–9056 (2020). https://doi.org/10.1039/d0cs00930j
6. J. Liu, D. Zheng, K. Wang, Z. Li, S. Liu et al., Evolutionary manufacturing approaches for advancing flexible perovskite solar cells. Joule **8**(4), 944–969 (2024). https://doi.org/10.1016/j.joule.2024.02.025
7. A. Kausar, A. Sattar, C. Xu, S. Zhang, Z. Kang et al., Advent of alkali metal doping: a roadmap for the evolution of perovskite solar cells. Chem. Soc. Rev. **50**(4), 2696–2736 (2021). https://doi.org/10.1039/d0cs01316a
8. C.-H. Lu, G.V. Biesold-McGee, Y. Liu, Z. Kang, Z. Lin, Doping and ion substitution in colloidal metal halide perovskite nanocrystals. Chem. Soc. Rev. **49**(14), 4953–5007 (2020). https://doi.org/10.1039/c9cs00790c
9. A. Dey, J. Ye, A. De, E. Debroye, S.K. Ha et al., State of the art and prospects for halide perovskite nanocrystals. ACS Nano **15**(7), 10775–10981 (2021). https://doi.org/10.1021/acsnano.0c08903
10. J. Wang, Y. Shi, Y. Wang, Z. Li, Rational design of metal halide perovskite nanocrystals for photocatalytic CO_2 reduction: recent advances, challenges, and prospects. ACS Energy Lett. **7**(6), 2043–2059 (2022). https://doi.org/10.1021/acsenergylett.2c00752
11. S. Park, W.J. Chang, C.W. Lee, S. Park, H.-Y. Ahn et al., Photocatalytic hydrogen generation from hydriodic acid using methylammonium lead iodide in dynamic equilibrium with aqueous solution. Nat. Energy **2**, 16185 (2017). https://doi.org/10.1038/nenergy.2016.185
12. C. Zhao, H. Song, Y. Chen, W. Xiong, M. Hu et al., Stable and recyclable photocatalysts of $CsPbBr_3$@MSNs nanocomposites for photoinduced electron transfer RAFT polymerization. ACS Energy Lett. **7**(12), 4389–4397 (2022). https://doi.org/10.1021/acsenergylett.2c02293
13. Y. Dong, Y. Feng, Z. Li, H. Zhou, H. Lv et al., $CsPbBr_3$/Polyoxometalate composites for selective photocatalytic oxidation of benzyl alcohol. ACS Catal. **13**, 14346 (2023). https://doi.org/10.1021/acscatal.3c03977
14. M. Liu, P. Xia, G. Zhao, C. Nie, K. Gao et al., Energy-transfer photocatalysis using lead halide perovskite nanocrystals: sensitizing molecular isomerization and cycloaddition. Angew. Chem. Int. Ed. **61**(35), e202208241 (2022). https://doi.org/10.1002/anie.202208241
15. K. Ren, S. Yue, C. Li, Z. Fang, K.A.M. Gasem et al., Metal halide perovskites for photocatalysis applications. J. Mater. Chem. A **10**(2), 407–429 (2022). https://doi.org/10.1039/d1ta09148d
16. N. Li, X. Chen, J. Wang, X. Liang, L. Ma et al., ZnSe nanorods-$CsSnCl_3$ perovskite heterojunction composite for photocatalytic CO_2 reduction. ACS Nano **16**(2), 3332–3340 (2022). https://doi.org/10.1021/acsnano.1c11442
17. Z. Liu, H. Yang, J. Wang, Y. Yuan, K. Hills-Kimball et al., Synthesis of lead-free Cs(2)AgBiX(6) (X = Cl, Br, I) double perovskite nanoplatelets and their application in CO_2 photocatalytic reduction. Nano Lett. **21**(4), 1620–1627 (2021). https://doi.org/10.1021/acs.nanolett.0c04148
18. S. Pan, J. Li, Z. Wen, R. Lu, Q. Zhang et al., Halide perovskite materials for photo(electro)chemical applications: dimensionality, heterojunction, and performance. Adv. Energy Mater. **12**(4), 2004002 (2022). https://doi.org/10.1002/aenm.202004002
19. L. Li, Z. Zhang, *In-situ* fabrication of Cu doped dual-phase $CsPbBr_3$–Cs_4PbBr_6 inorganic perovskite nanocomposites for efficient and selective photocatalytic CO_2 reduction. Chem. Eng. J. **434**, 134811 (2022). https://doi.org/10.1016/j.cej.2022.134811
20. J. Wang, L. Xiong, Y. Bai, Z. Chen, Q. Zheng et al., Mn-doped perovskite nanocrystals for photocatalytic CO_2 reduction: insight into the role of the charge carriers with

prolonged lifetime. Solar RRL **6**(8), 2270086 (2022). https://doi.org/10.1002/solr.202270086

21. X.-D. Wang, Y.-H. Huang, J.-F. Liao, Y. Jiang, L. Zhou et al., *In situ* construction of a Cs_2SnI_6 perovskite nanocrystal/SnS_2 nanosheet heterojunction with boosted interfacial charge transfer. J. Am. Chem. Soc. **141**(34), 13434–13441 (2019). https://doi.org/10.1021/jacs.9b04482
22. Q. Guo, J.-D. Zhang, Y.-J. Chen, K.-Y. Zhang, L.-N. Guo et al., Enhanced hydrogen evolution activity of $CsPbBr_3$ nanocrystals achieved by dimensionality change. Chem. Commun. **59**(28), 4189–4192 (2023). https://doi.org/10.1039/D2CC06731E
23. Q. Guo, J.-D. Zhang, J.-M. Liu, Y.-J. Chen, B. Qin et al., Promoting charge-carriers dynamics by relaxed lattice strain in A-site-doped halide perovskite for photocatalytic H_2 evolution. Angew. Chem. Int. Ed. **64**(5), e202419082 (2025). https://doi.org/10.1002/anie.202419082
24. Q. Guo, J.-L. Lu, B. Qin, Q.-C. Shan, L. Liu et al., Facets in metal halide perovskite nanocrystals for the photoinduced electron transfer annulation reaction. J. Mater. Chem. A **12**(35), 23406–23410 (2024). https://doi.org/10.1039/D4TA04268A
25. Y. Li, J. Zhang, Q. Chen, X. Xia, M. Chen, Emerging of heterostructure materials in energy storage: a review. Adv. Mater. **33**(27), 2100855 (2021). https://doi.org/10.1002/adma.202100855
26. J. Chen, D. Yuan, Y. Wang, Covalent organic frameworks based heterostructure in solar-to-fuel conversion. Adv. Funct. Mater. **33**(41), 2304071 (2023). https://doi.org/10.1002/adfm.202304071
27. Q. Guo, X. Feng, Z.C. Zhang, L. Huang, Interfacial interactions between co-based cocatalysts and semiconducting light absorbers for solar-light-driven redox reactions. Sol. RRL **5**(8), 2100234 (2021). https://doi.org/10.1002/solr.202100234
28. D. Huang, S. Chen, G. Zeng, X. Gong, C. Zhou et al., Artificial Z-scheme photocatalytic system: what have been done and where to go? Coord. Chem. Rev. **385**, 44–80 (2019). https://doi.org/10.1016/j.ccr.2018.12.013
29. X. Li, J. Yu, M. Jaroniec, X. Chen, Cocatalysts for selective photoreduction of CO_2 into solar fuels. Chem. Rev. **119**(6), 3962–4179 (2019). https://doi.org/10.1021/acs.chemrev.8b00400
30. J. Low, J. Yu, M. Jaroniec, S. Wageh, A.A. Al-Ghamdi, Heterojunction photocatalysts. Adv. Mater. **29**(20), 1601694 (2017). https://doi.org/10.1002/adma.201601694
31. M. Lin, H. Chen, Z. Zhang, X. Wang, Engineering interface structures for heterojunction photocatalysts. Phys. Chem. Chem. Phys. **25**(6), 4388–4407 (2023). https://doi.org/10.1039/d2cp05281d
32. H. Wang, L. Zhang, Z. Chen, J. Hu, S. Li et al., Semiconductor heterojunction photocatalysts: design, construction, and photocatalytic performances. Chem. Soc. Rev. **43**(15), 5234 (2014). https://doi.org/10.1039/c4cs00126e
33. Y. Tong, W. Liu, C. Li, X. Liu, J. Liu et al., A metal/semiconductor contact induced Mott-Schottky junction for enhancing the electrocatalytic activity of water-splitting catalysts. Sustain. Energy Fuels **7**(1), 12–30 (2022). https://doi.org/10.1039/d2se01355j
34. Y. Wu, P. Wang, Z. Guan, J. Liu, Z. Wang et al., Enhancing the photocatalytic hydrogen evolution activity of mixed-halide perovskite $CH_3NH_3PbBr_{3-x}I_x$ achieved by bandgap funneling of charge carriers. ACS Catal. **8**(11), 10349–10357 (2018). https://doi.org/10.1021/acscatal.8b02374
35. Q. Zhang, M. Tai, Y. Zhou, Y. Zhou, Y. Wei et al., Enhanced photocatalytic property of γ-$CsPbI_3$ perovskite nanocrystals with WS_2. ACS Sustain. Chem. Eng. **8**(2), 1219–1229 (2020). https://doi.org/10.1021/acssuschemeng.9b06451
36. Z. Zhang, B. Wang, H.-B. Zhao, J.-F. Liao, Z.-C. Zhou et al., Self-assembled lead-free double perovskite-MXene heterostructure with efficient charge separation for photocatalytic CO_2 reduction. Appl. Catal. B Environ. **312**, 121358 (2022). https://doi.org/10.1016/j.apcatb.2022.121358
37. W. Li, F. Wang, Z. Zhang, S. Min, $MAPbI_3$ microcrystals integrated with $Ti_3C_2T_x$ MXene nanosheets for efficient visible-light photocatalytic H_2 evolution. Chem. Commun. **57**(63), 7774–7777 (2021). https://doi.org/10.1039/D1CC02511B
38. Q. Guo, F. Liang, X.-Y. Gao, Q.-C. Gan, X.-B. Li et al., Metallic Co_2C: a promising co-catalyst to boost photocatalytic hydrogen evolution of colloidal quantum dots. ACS Catal. **8**(7), 5890–5895 (2018). https://doi.org/10.1021/acscatal.8b01105
39. Z. Zhao, J. Wu, Y.-Z. Zheng, N. Li, X. Li et al., Ni_3C-decorated $MAPbI_3$ as visible-light photocatalyst for H_2 evolution from HI splitting. ACS Catal. **9**(9), 8144–8152 (2019). https://doi.org/10.1021/acscatal.9b01605
40. X.-B. Li, C.-H. Tung, L.-Z. Wu, Semiconducting quantum dots for artificial photosynthesis. Nat. Rev. Chem. **2**(8), 160–173 (2018). https://doi.org/10.1038/s41570-018-0024-8
41. D. Xiang, F. Niu, J. Ji, J. Liang, H. Chen et al., Construction of graphene supported dual-phase perovskite quantum dots for efficient photocatalytic CO_2 reduction. J. Mol. Struct. **1295**, 136711 (2024). https://doi.org/10.1016/j.molstruc.2023.136711
42. X. Wang, J. He, J. Li, G. Lu, F. Dong et al., Immobilizing perovskite $CsPbBr_3$ nanocrystals on black phosphorus nanosheets for boosting charge separation and photocatalytic CO_2 reduction. Appl. Catal. B Environ. **277**, 119230 (2020). https://doi.org/10.1016/j.apcatb.2020.119230
43. B. Zhu, B. Cheng, J. Fan, W. Ho, J. Yu, G-C_3N_4-based 2D/2D composite heterojunction photocatalyst. Small Struct. **2**(12), 2100086 (2021). https://doi.org/10.1002/sstr.202100086
44. J. Wang, I. Mora-Seró, Z. Pan, K. Zhao, H. Zhang et al., Core/shell colloidal quantum dot exciplex states for the development of highly efficient quantum-dot-sensitized solar cells. J. Am. Chem. Soc. **135**(42), 15913–15922 (2013). https://doi.org/10.1021/ja4079804
45. Y. Yang, Z. Chen, H. Huang, Y. Liu, J. Zou et al., Synergistic surface activation during photocatalysis on perovskite derivative sites in heterojunction. Appl. Catal. B Environ.

323, 122146 (2023). https://doi.org/10.1016/j.apcatb.2022.122146

46. B.-J. Ng, L.K. Putri, X.Y. Kong, Y.W. Teh, P. Pasbakhsh et al., Z-scheme photocatalytic systems for solar water splitting. Adv. Sci. **7**(7), 1903171 (2020). https://doi.org/10.1002/advs.201903171
47. A. Kumar, P. Singh, V.-H. Nguyen, Q.V. Le, T. Ahamad et al., Rationally constructed synergy between dual-vacancies and Z-scheme heterostructured MoS_{2-x}/g-C_3N_4/Ca-α-Fe_2O_3 for high-performance photodegradation of sulfamethoxazole antibiotic from aqueous solution. Chem. Eng. J. **474**, 145720 (2023). https://doi.org/10.1016/j.cej.2023.145720
48. M.E. Malefane, P.J. Mafa, M. Managa, T.T.I. Nkambule, A.T. Kuvarega, Understanding the principles and applications of dual Z-scheme heterojunctions: how far can we go? J. Phys. Chem. Lett. **14**(4), 1029–1045 (2023). https://doi.org/10.1021/acs.jpclett.2c03387
49. Y. Wang, H. Huang, Z. Zhang, C. Wang, Y. Yang et al., Lead-free perovskite $Cs_2AgBiBr_6$@g-C_3N_4 Z-scheme system for improving CH_4 production in photocatalytic CO_2 reduction. Appl. Catal. B Environ. **282**, 119570 (2021). https://doi.org/10.1016/j.apcatb.2020.119570
50. L. Zhang, J. Zhang, H. Yu, J. Yu, Emerging S-scheme photocatalyst. Adv. Mater. **34**(11), 2107668 (2022). https://doi.org/10.1002/adma.202107668
51. Q. Xu, L. Zhang, B. Cheng, J. Fan, J. Yu, S-scheme heterojunction photocatalyst. Chem **6**(7), 1543–1559 (2020). https://doi.org/10.1016/j.chempr.2020.06.010
52. Y. Bao, S. Song, G. Yao, S. Jiang, S-scheme photocatalytic systems. Sol. RRL **5**(7), 2100118 (2021). https://doi.org/10.1002/solr.202100118
53. X. Yue, L. Cheng, J. Fan, Q. Xiang, 2D/2D $BiVO_4$/$CsPbBr_3$ s-scheme heterojunction for photocatalytic CO_2 reduction: insights into structure regulation and Fermi level modulation. Appl. Catal. B Environ. **304**, 120979 (2022). https://doi.org/10.1016/j.apcatb.2021.120979
54. J. Wang, J. Wang, N. Li, X. Du, J. Ma et al., Direct Z-scheme 0D/2D heterojunction of $CsPbBr_3$ quantum dots/Bi_2WO_6 nanosheets for efficient photocatalytic CO_2 reduction. ACS Appl. Mater. Interf. **12**(28), 31477–31485 (2020). https://doi.org/10.1021/acsami.0c08152
55. L. Li, Z. Zhang, C. Ding, J. Xu, Boosting charge separation and photocatalytic CO_2 reduction of $CsPbBr_3$ perovskite quantum dots by hybridizing with P3HT. Chem. Eng. J. **419**, 129543 (2021). https://doi.org/10.1016/j.cej.2021.129543
56. Z. Zhang, L. Li, Y. Jiang, J. Xu, Step-scheme photocatalyst of $CsPbBr_3$ quantum dots/BiOBr nanosheets for efficient CO_2 photoreduction. Inorg. Chem. **61**(7), 3351–3360 (2022). https://doi.org/10.1021/acs.inorgchem.2c00012
57. Z. Zhang, Z. Dong, Y. Jiang, Y. Chu, J. Xu, A novel S-scheme heterojunction of $CsPbBr_3$ nanocrystals/AgBr nanorods for artificial photosynthesis. Chem. Eng. J. **435**, 135014 (2022). https://doi.org/10.1016/j.cej.2022.135014
58. Y. Wu, X. Yue, J. Fan, X. Hao, Q. Xiang, *In situ* fabrication of plasmonic Bi/$CsPbBr_3$ composite photocatalyst toward enhanced photocatalytic CO_2 reduction. Appl. Surf. Sci. **609**, 155391 (2023). https://doi.org/10.1016/j.apsusc.2022.155391
59. S.-R. Xu, J.-L. Li, Q.-L. Mo, K. Wang, G. Wu et al., Steering photocatalytic CO_2 conversion over $CsPbBr_3$ perovskite nanocrystals by coupling with transition-metal chalcogenides. Inorg. Chem. **61**(44), 17828–17837 (2022). https://doi.org/10.1021/acs.inorgchem.2c03148
60. Y. Jiang, Y. Wang, Z. Zhang, Z. Dong, J. Xu, 2D/2D $CsPbBr_3$/BiOCl heterojunction with an S-scheme charge transfer for boosting the photocatalytic conversion of CO_2. Inorg. Chem. **61**(27), 10557–10566 (2022). https://doi.org/10.1021/acs.inorgchem.2c01452
61. Q. Wang, J. Wang, J.-C. Wang, X. Hu, Y. Bai et al., Coupling $CsPbBr_3$ quantum dots with covalent triazine frameworks for visible-light-driven CO_2 reduction. Chemsuschem **14**(4), 1131–1139 (2021). https://doi.org/10.1002/cssc.202002847
62. Y. Wang, J. Wang, M. Zhang, S. Zheng, J. Wu et al., In situ constructed perovskite-chalcogenide heterojunction for photocatalytic CO_2 reduction. Small **19**(37), e2300841 (2023). https://doi.org/10.1002/smll.202300841
63. H. Huang, J. Zhao, Y. Du, C. Zhou, M. Zhang et al., Direct Z-scheme heterojunction of semicoherent $FAPbBr_3$/Bi_2WO_6 interface for photoredox reaction with large driving force. ACS Nano **14**(12), 16689–16697 (2020). https://doi.org/10.1021/acsnano.0c03146
64. L. Romani, A. Speltini, F. Ambrosio, E. Mosconi, A. Profumo et al., Water-stable $DMASnBr_3$ lead-free perovskite for effective solar-driven photocatalysis. Angew. Chem. Int. Ed. **60**(7), 3611–3618 (2021). https://doi.org/10.1002/anie.202007584
65. Z.-C. Kong, J.-F. Liao, Y.-J. Dong, Y.-F. Xu, H.-Y. Chen et al., Core@Shell $CsPbBr_3$@Zeolitic imidazolate framework nanocomposite for efficient photocatalytic CO_2 reduction. ACS Energy Lett. **3**(11), 2656–2662 (2018). https://doi.org/10.1021/acsenergylett.8b01658
66. H. Hu, W. Guan, Y. Xu, X. Wang, L. Wu et al., Construction of single-atom platinum catalysts enabled by $CsPbBr_3$ nanocrystals. ACS Nano **15**(8), 13129–13139 (2021). https://doi.org/10.1021/acsnano.1c02515
67. K. Su, G.-X. Dong, W. Zhang, Z.-L. Liu, M. Zhang et al., *In situ* coating $CsPbBr_3$ nanocrystals with graphdiyne to boost the activity and stability of photocatalytic CO_2 reduction. ACS Appl. Mater. Interf. **12**(45), 50464–50471 (2020). https://doi.org/10.1021/acsami.0c14826
68. R. Cheng, J.A. Steele, M.B.J. Roeffaers, J. Hofkens, E. Debroye, Dual-channel charge carrier transfer in $CsPbX_3$ perovskite/$W_{18}O_{49}$ composites for selective photocatalytic benzyl alcohol oxidation. ACS Appl. Energy Mater. **4**(4), 3460–3468 (2021). https://doi.org/10.1021/acsaem.0c03215
69. Y. Tang, C.H. Mak, R. Liu, Z. Wang, L. Ji et al., *In situ* formation of bismuth-based perovskite heterostructures for high-performance cocatalyst-free photocatalytic hydrogen evolution. Adv. Funct. Mater. **30**(52), 2006919 (2020). https://doi.org/10.1002/adfm.202006919
70. L. Ding, B. Borjigin, Y. Li, X. Yang, X. Wang et al., Assembling an affinal 0D $CsPbBr_3$/2D $CsPb_2Br_5$ architecture by synchronously in situ growing $CsPbBr_3$ QDs and $CsPb_2Br_5$

 https://doi.org/10.1007/s40820-025-01886-y

nanosheets: enhanced activity and reusability for photocatalytic CO_2 reduction. ACS Appl. Mater. Interf. **13**(43), 51161–51173 (2021). https://doi.org/10.1021/acsami.1c17870

71. N. Kandoth, S.P. Chaudhary, S. Gupta, K. Raksha, A. Chatterjee et al., Multimodal biofilm inactivation using a photocatalytic bismuth perovskite–TiO_2–Ru(II)polypyridyl-based multisite heterojunction. ACS Nano **17**(11), 10393–10406 (2023). https://doi.org/10.1021/acsnano.3c01064
72. Y.-F. Mu, W. Zhang, G.-X. Dong, K. Su, M. Zhang et al., Ultrathin and small-size graphene oxide as an electron mediator for perovskite-based Z-scheme system to significantly enhance photocatalytic CO_2 reduction. Small **16**(29), 2002140 (2020). https://doi.org/10.1002/smll.202002140
73. Q. Guo, F. Liang, Z. Sun, Y. Wang, X.-B. Li et al., Optimal d-band-induced Cu_3N as a cocatalyst on metal sulfides for boosting photocatalytic hydrogen evolution. J. Mater. Chem. A **8**(43), 22601–22606 (2020). https://doi.org/10.1039/D0TA07916B
74. X.-Z. Wang, S.-L. Meng, J. Liu, C. Yu, C. Ye et al., Mechanistic insights into consecutive 2e− and 2H+ reactions of hydrogenase mimic. Chem **9**(9), 2610–2619 (2023). https://doi.org/10.1016/j.chempr.2023.05.010
75. B. Li, W. Wang, J. Zhao, Z. Wang, B. Su et al., All-solid-state direct Z-scheme $NiTiO_3/Cd_{0.5}Zn_{0.5}S$ heterostructures for photocatalytic hydrogen evolution with visible light. J. Mater. Chem. A **9**(16), 10270–10276 (2021). https://doi.org/10.1039/d1ta01220g
76. J. Li, F. University, J. Zhao, F. University, S. Wang et al., Activating lattice oxygen in perovskite ferrite for efficient and stable photothermal dry reforming of methane. J. Am. Chem. Soc. **147**(17), 14705–14714 (2025). https://doi.org/10.1021/jacs.5c03098
77. P. Zhou, H. Chen, Y. Chao, Q. Zhang, W. Zhang et al., Single-atom Pt-I_3 sites on all-inorganic Cs_2SnI_6 perovskite for efficient photocatalytic hydrogen production. Nat. Commun. **12**(1), 4412 (2021). https://doi.org/10.1038/s41467-021-24702-8
78. C. Cai, Y. Teng, J.-H. Wu, J.-Y. Li, H.-Y. Chen et al., *In situ* photosynthesis of an $MAPbI_3$/CoP hybrid heterojunction for efficient photocatalytic hydrogen evolution. Adv. Funct. Mater. **30**(35), 2001478 (2020). https://doi.org/10.1002/adfm.202001478
79. H. Zhao, K. Chordiya, P. Leukkunen, A. Popov, M. Upadhyay Kahaly et al., Dimethylammonium iodide stabilized bismuth halide perovskite photocatalyst for hydrogen evolution. Nano Res. **14**(4), 1116–1125 (2021). https://doi.org/10.1007/s12274-020-3159-0
80. Y. Jiang, K. Li, X. Wu, M. Zhu, H. Zhang et al., *In situ* synthesis of lead-free halide perovskite $Cs_2AgBiBr_6$ supported on nitrogen-doped carbon for efficient hydrogen evolution in aqueous HBr solution. ACS Appl. Mater. Interf. **13**(8), 10037–10046 (2021). https://doi.org/10.1021/acsami.0c21588
81. Y. Wu, P. Wang, X. Zhu, Q. Zhang, Z. Wang et al., Composite of $CH_3NH_3PbI_3$ with reduced graphene oxide as a highly efficient and stable visible-light photocatalyst for hydrogen evolution in aqueous HI solution. Adv. Mater. **30**(7), 1704342 (2018). https://doi.org/10.1002/adma.201704342
82. R. Li, X. Li, J. Wu, X. Lv, Y.-Z. Zheng et al., Few-layer black phosphorus-on-$MAPbI_3$ for superb visible-light photocatalytic hydrogen evolution from HI splitting. Appl. Catal. B Environ. **259**, 118075 (2019). https://doi.org/10.1016/j.apcatb.2019.118075
83. L. Romani, A. Speltini, C.N. Dibenedetto, A. Listorti, F. Ambrosio et al., Experimental strategy and mechanistic view to boost the photocatalytic activity of $Cs_3Bi_2Br_9$ lead-free perovskite derivative by g-C_3N_4 composite engineering. Adv. Funct. Mater. **31**(46), 2104428 (2021). https://doi.org/10.1002/adfm.202104428
84. X. Zhao, S. Chen, H. Yin, S. Jiang, K. Zhao et al., Perovskite microcrystals with intercalated monolayer MoS_2 nanosheets as advanced photocatalyst for solar-powered hydrogen generation. Matter **3**(3), 935–949 (2020). https://doi.org/10.1016/j.matt.2020.07.004
85. X. Wang, H. Wang, H. Zhang, W. Yu, X. Wang et al., Dynamic interaction between methylammonium lead iodide and TiO_2 nanocrystals leads to enhanced photocatalytic H_2 evolution from HI splitting. ACS Energy Lett. **3**(5), 1159–1164 (2018). https://doi.org/10.1021/acsenergylett.8b00488
86. H. Lv, H. Yin, N. Jiao, C. Yuan, S. Weng et al., Efficient charge transfer and effective active sites in lead-free halide double perovskite S-scheme heterojunctions for photocatalytic H_2 evolution. Small Methods. **7**(3), 2201365 (2023). https://doi.org/10.1002/smtd.202201365
87. Y. Guo, G. Liu, Z. Li, Y. Lou, J. Chen et al., Stable lead-free $(CH_3NH_3)_3Bi_2I_9$ perovskite for photocatalytic hydrogen generation. ACS Sustainable Chem. Eng. **7**(17), 15080–15085 (2019). https://doi.org/10.1021/acssuschemeng.9b03761
88. Q. Huang, Y. Guo, J. Chen, Y. Lou, Y. Zhao, NiCoP modified lead-free double perovskite $Cs_2AgBiBr_6$ for efficient photocatalytic hydrogen generation. New J. Chem. **46**(16), 7395–7402 (2022). https://doi.org/10.1039/d2nj00435f
89. H. Fu, Q. Zhang, Y. Wu, Z. Wang, Y. Liu et al., Composite of mixed-cation perovskite MA1-FA PbI_3 with $MoSe_2$ for enhanced photocatalytic H_2 evolution. Chem. Eng. J. **511**, 162120 (2025). https://doi.org/10.1016/j.cej.2025.162120
90. K. Song, J. Gou, L. Wu, C. Zeng, Two-dimensional black phosphorus-modified $Cs_2AgBiBr_6$ with efficient charge separation for enhanced visible-light photocatalytic H_2 evolution. J. Mater. Chem. C **10**(41), 15386–15393 (2022). https://doi.org/10.1039/d2tc03100k
91. J. Cai, X. Li, B. Su, B. Guo, X. Lin et al., Rational design and fabrication of S-scheme $NiTiO_3$/CdS heterostructures for photocatalytic CO_2 reduction. J. Mater. Sci. Technol. **234**, 82–89 (2025). https://doi.org/10.1016/j.jmst.2025.01.050
92. B. Su, H. Huang, Z. Ding, M.B.J. Roeffaers, S. Wang et al., S-scheme $CoTiO_3/Cd_{9.51}Zn_{0.49}S_{10}$ heterostructures for visible-light driven photocatalytic CO_2 reduction. J. Mater. Sci. Technol. **124**, 164–170 (2022). https://doi.org/10.1016/j.jmst.2022.01.030

93. Q. Guo, F. Liang, X.-B. Li, Y.-J. Gao, M.-Y. Huang et al., Efficient and selective CO_2 reduction integrated with organic synthesis by solar energy. Chem **5**(10), 2605–2616 (2019). https://doi.org/10.1016/j.chempr.2019.06.019
94. Q. Guo, S.-G. Xia, Z.-K. Xin, Y. Wang, F. Liang et al., Anion vacancy correlated photocatalytic CO_2 to CO conversion over quantum-confined CdS nanorods under visible light. J. Mater. Chem. A **11**(8), 3937–3941 (2023). https://doi.org/10.1039/D2TA09451G
95. K. Li, B. Peng, T. Peng, Recent advances in heterogeneous photocatalytic CO_2 conversion to solar fuels. ACS Catal. **6**(11), 7485–7527 (2016). https://doi.org/10.1021/acscatal.6b02089
96. J. Ran, M. Jaroniec, S.-Z. Qiao, Cocatalysts in semiconductor-based photocatalytic CO_2 reduction: achievements, challenges, and opportunities. Adv. Mater. **30**(7), 1704649 (2018). https://doi.org/10.1002/adma.201704649
97. Y.-F. Xu, M.-Z. Yang, B.-X. Chen, X.-D. Wang, H.-Y. Chen et al., A $CsPbBr_3$ perovskite quantum dot/graphene oxide composite for photocatalytic CO_2 reduction. J. Am. Chem. Soc. **139**(16), 5660–5663 (2017). https://doi.org/10.1021/jacs.7b00489
98. H.-B. Zhao, J.-N. Huang, Q. Qin, H.-Y. Chen, D.-B. Kuang, *In situ* loading of Cu nanocrystals on $CsCuCl_3$ for selective photoreduction of CO_2 to CH_4. Small **19**(45), 2302022 (2023). https://doi.org/10.1002/smll.202302022
99. Y.-F. Xu, M.-Z. Yang, H.-Y. Chen, J.-F. Liao, X.-D. Wang et al., Enhanced solar-driven gaseous CO_2 conversion by $CsPbBr_3$ nanocrystal/Pd nanosheet Schottky-junction photocatalyst. ACS Appl. Energy Mater. **1**(9), 5083–5089 (2018). https://doi.org/10.1021/acsaem.8b01133
100. M. Shu, Z. Zhang, Z. Dong, J. Xu, $CsPbBr_3$ perovskite quantum dots anchored on multiwalled carbon nanotube for efficient CO_2 photoreduction. Carbon **182**, 454–462 (2021). https://doi.org/10.1016/j.carbon.2021.06.040
101. A. Pan, X. Ma, S. Huang, Y. Wu, M. Jia et al., $CsPbBr_3$ perovskite nanocrystal grown on MXene nanosheets for enhanced photoelectric detection and photocatalytic CO_2 reduction. J. Phys. Chem. Lett. **10**(21), 6590–6597 (2019). https://doi.org/10.1021/acs.jpclett.9b02605
102. M. Que, Y. Zhao, Y. Yang, L. Pan, W. Lei et al., Anchoring of formamidinium lead bromide quantum dots on Ti_3C_2 nanosheets for efficient photocatalytic reduction of CO_2. ACS Appl. Mater. Interf. **13**(5), 6180–6187 (2021). https://doi.org/10.1021/acsami.0c18391
103. X. Wang, J. He, L. Mao, X. Cai, C. Sun et al., $CsPbBr_3$ perovskite nanocrystals anchoring on monolayer MoS_2 nanosheets for efficient photocatalytic CO_2 reduction. Chem. Eng. J. **416**, 128077 (2021). https://doi.org/10.1016/j.cej.2020.128077
104. L. Ding, F. Bai, B. Borjigin, Y. Li, H. Li et al., Embedding $Cs_2AgBiBr_6$ QDs into Ce-UiO-66-H to *in situ* construct a novel bifunctional material for capturing and photocatalytic reduction of CO_2. Chem. Eng. J. **446**, 137102 (2022). https://doi.org/10.1016/j.cej.2022.137102
105. W. Xiong, Y. Dong, A. Pan, Fabricating a type II heterojunction by growing lead-free perovskite $Cs_2AgBiBr_6$ in situ on graphite-like g-C_3N_4 nanosheets for enhanced photocatalytic CO_2 reduction. Nanoscale **15**(38), 15619–15625 (2023). https://doi.org/10.1039/d3nr04152b
106. M. Ou, W. Tu, S. Yin, W. Xing, S. Wu et al., Amino-assisted anchoring of $CsPbBr_3$ perovskite quantum dots on porous g-C_3N_4 for enhanced photocatalytic CO_2 reduction. Angew. Chem. Int. Ed. **57**(41), 13570–13574 (2018). https://doi.org/10.1002/anie.201808930
107. Y. Jiang, J.-F. Liao, H.-Y. Chen, H.-H. Zhang, J.-Y. Li et al., All-solid-state Z-scheme α-Fe_2O_3/amine-RGO/$CsPbBr_3$ hybrids for visible-light-driven photocatalytic CO_2 reduction. Chem **6**(3), 766–780 (2020). https://doi.org/10.1016/j.chempr.2020.01.005
108. Y.-F. Mu, C. Zhang, M.-R. Zhang, W. Zhang, M. Zhang et al., Direct Z-scheme heterojunction of ligand-free $FAPbBr_3$/α-Fe_2O_3 for boosting photocatalysis of CO_2 reduction coupled with water oxidation. ACS Appl. Mater. Interf. **13**(19), 22314–22322 (2021). https://doi.org/10.1021/acsami.1c01718
109. R. Zhang, L. Li, Y. Li, D. Wang, Y. Lin et al., Z-scheme SnS_2/$CsPbBr_3$ heterojunctions for photoreduction CO_2 reaction and related photoinduced carrier behaviors. Solar RRL **6**(10), 2200536 (2022). https://doi.org/10.1002/solr.202200536
110. H. Sun, R. Tang, X. Zhang, S. Zhang, W. Yang et al., Interfacial energy band engineered $CsPbBr_3$/NiFe-LDH heterostructure catalysts with tunable visible light driven photocatalytic CO_2 reduction capability. Catal. Sci. Technol. **13**(4), 1154–1163 (2023). https://doi.org/10.1039/d2cy01982e
111. P. Wang, X. Ba, X. Zhang, H. Gao, M. Han et al., Direct Z-scheme heterojunction of PCN^-222/$CsPbBr_3$ for boosting photocatalytic CO_2 reduction to HCOOH. Chem. Eng. J. **457**, 141248 (2023). https://doi.org/10.1016/j.cej.2022.141248
112. Z.-L. Liu, R.-R. Liu, Y.-F. Mu, Y.-X. Feng, G.-X. Dong et al., *In situ* construction of lead-free perovskite direct Z-scheme heterojunction $Cs_3Bi_2I_9$/Bi_2WO_6 for efficient photocatalysis of CO_2 reduction. Solar RRL **5**(3), 2000691 (2021). https://doi.org/10.1002/solr.202000691
113. X. Wang, Z. Wang, Y. Li, J. Wang, G. Zhang, Efficient photocatalytic CO_2 conversion over 2D/2D Ni-doped $CsPbBr_3$/Bi_3O_4Br Z-scheme heterojunction: critical role of Ni doping, boosted charge separation and mechanism study. Appl. Catal. B Environ. **319**, 121895 (2022). https://doi.org/10.1016/j.apcatb.2022.121895
114. L. Ding, Y. Ding, F. Bai, G. Chen, S. Zhang et al., *In situ* growth of $Cs_3Bi_2Br_9$ quantum dots on Bi-MOF nanosheets *via* cosharing bismuth atoms for CO_2 capture and photocatalytic reduction. Inorg. Chem. **62**(5), 2289–2303 (2023). https://doi.org/10.1021/acs.inorgchem.2c04041
115. Q.-M. Sun, J.-J. Xu, F.-F. Tao, W. Ye, C. Zhou et al., Boosted inner surface charge transfer in perovskite Nanodots@mesoporous titania frameworks for efficient and selective photocatalytic CO_2 reduction to methane. Angew. Chem. Int.

 https://doi.org/10.1007/s40820-025-01886-y

Ed. **61**(20), e202200872 (2022). https://doi.org/10.1002/anie.202200872

116. P. Hu, G. Liang, B. Zhu, W. Macyk, J. Yu et al., Highly selective photoconversion of CO_2 to CH_4 over $SnO_2/Cs_3Bi_2Br_9$ heterojunctions assisted by S-scheme charge separation. ACS Catal. **13**(19), 12623–12633 (2023). https://doi.org/10.1021/acscatal.3c03095
117. J.-N. Huang, Y.-J. Dong, H.-B. Zhao, H.-Y. Chen, D.-B. Kuang et al., Efficient encapsulation of $CsPbBr_3$ and Au nanocrystals in mesoporous metal–organic frameworks towards synergetic photocatalytic CO_2 reduction. J. Mater. Chem. A **10**(47), 25212–25219 (2022). https://doi.org/10.1039/d2ta06561d
118. X. Li, J. Liu, G. Jiang, X. Lin, J. Wang et al., Self-supported $CsPbBr/Ti_3C_2T_x$ MXene aerogels towards efficient photocatalytic CO_2 reduction. J. Colloid Interf. Sci. **643**, 174–182 (2023). https://doi.org/10.1016/j.jcis.2023.04.015
119. X. Wang, K. Li, J. He, J. Yang, F. Dong et al., Defect in reduced graphene oxide tailored selectivity of photocatalytic CO_2 reduction on Cs_4PbBr6 pervoskite hole-in-microdisk structure. Nano Energy **78**, 105388 (2020). https://doi.org/10.1016/j.nanoen.2020.105388
120. Z. Zhang, M. Shu, Y. Jiang, J. Xu, Fullerene modified $CsPbBr_3$ perovskite nanocrystals for efficient charge separation and photocatalytic CO_2 reduction. Chem. Eng. J. **414**, 128889 (2021). https://doi.org/10.1016/j.cej.2021.128889
121. Y. Jiang, C. Mei, Z. Zhang, Z. Dong, Immobilizing $CsPbBr_3$ perovskite nanocrystals on nanoporous carbon powder for visible-light-driven CO_2 photoreduction. Dalton Trans. **50**(45), 16711–16719 (2021). https://doi.org/10.1039/D1DT03099J
122. X. Zhong, X. Liang, X. Lin, J. Wang, M.Z. Shahid et al., A new 0D–2D $CsPbBr_3$–Co_3O_4 heterostructure photocatalyst with efficient charge separation for photocatalytic CO_2 reduction. Inorg. Chem. Front. **10**(11), 3273–3283 (2023). https://doi.org/10.1039/D3QI00527E
123. T.H. Kim, I. Park, K.H. Lee, J.-H. Sim, M.-H. Park et al., Investigating the interfacial properties of halide perovskite/TiOx heterostructures for versatile photocatalytic reactions under sunlight. Nanoscale **15**(17), 7710–7714 (2023). https://doi.org/10.1039/D2NR06840K
124. Y. Jiang, J.-F. Liao, Y.-F. Xu, H.-Y. Chen, X.-D. Wang et al., Hierarchical $CsPbBr_3$ nanocrystal-decorated ZnO nanowire/macroporous graphene hybrids for enhancing charge separation and photocatalytic CO_2 reduction. J. Mater. Chem. A **7**(22), 13762–13769 (2019). https://doi.org/10.1039/c9ta03478a
125. G. Yin, X. Qi, Y. Chen, Q. Peng, X. Jiang et al., Constructing an all zero-dimensional $CsPbBr_3$/CdSe heterojunction for highly efficient photocatalytic CO_2 reduction. J. Mater. Chem. A **10**(42), 22468–22476 (2022). https://doi.org/10.1039/d2ta05186a
126. Q. Zheng, J. Wang, X. Li, Y. Bai, Y. Li et al., Surface halogen compensation on $CsPbBr_3$ nanocrystals with $SOBr_2$ for photocatalytic CO_2 reduction. ACS Mater. Lett. **4**(9), 1638–1645 (2022). https://doi.org/10.1021/acsmaterialslett.2c00482
127. Y.-X. Feng, G.-X. Dong, K. Su, Z.-L. Liu, W. Zhang et al., Self-template-oriented synthesis of lead-free perovskite $Cs_3Bi_2I_9$ nanosheets for boosting photocatalysis of CO_2 reduction over Z-scheme heterojunction $Cs_3Bi_2I_9/CeO_2$. J. Energy Chem. **69**, 348–355 (2022). https://doi.org/10.1016/j.jechem.2022.01.015
128. X. Jiang, Y. Ding, S. Zheng, Y. Ye, Z. Li et al., *In-situ* generated $CsPbBr_3$ nanocrystals on O-defective WO_3 for photocatalytic CO_2 reduction. Chemsuschem **15**(4), e202102295 (2022). https://doi.org/10.1002/cssc.202102295
129. A. Mahmoud Idris, S. Zheng, L. Wu, S. Zhou, H. Lin et al., A heterostructure of halide and oxide double perovskites $Cs_2AgBiBr_6/Sr_2FeNbO_6$ for boosting the charge separation toward high efficient photocatalytic CO_2 reduction under visible-light irradiation. Chem. Eng. J. **446**, 137197 (2022). https://doi.org/10.1016/j.cej.2022.137197
130. Y. Hou, Y. Zhang, S. Jiao, J. Qin, L. Liu et al., High catalytic activity and stability of visible-light-driven CO_2 reduction via $CsPbBr_3$ QDs/Cu-BTC core–shell photocatalysts. J. Mater. Chem. A **13**(7), 5007–5016 (2025). https://doi.org/10.1039/d4ta07190e
131. Y. Wang, Z. Liu, X. Tang, P. Huo, Z. Zhu et al., Construction of a $CsPbBr_3$ modified porous g-C_3N_4 photocatalyst for effective reduction of CO_2 and mechanism exploration. New J. Chem. **45**(2), 1082–1091 (2021). https://doi.org/10.1039/d0nj04018e
132. F. Xu, K. Meng, B. Cheng, S. Wang, J. Xu et al., Unique S-scheme heterojunctions in self-assembled $TiO_2/CsPbBr_3$ hybrids for CO_2 photoreduction. Nat. Commun. **11**(1), 4613 (2020). https://doi.org/10.1038/s41467-020-18350-7
133. L. Wang, J. Qiu, N. Wu, X. Yu, X. An, $TiO_2/CsPbBr_3$ S-scheme heterojunctions with highly improved CO_2 photoreduction activity through facet-induced Fermi level modulation. J. Colloid Interf. Sci. **629**, 206–214 (2023). https://doi.org/10.1016/j.jcis.2022.08.120
134. Y. Zhang, L. Shi, H. Yuan, X. Sun, X. Li et al., Construction of melamine foam–supported $WO_3/CsPbBr_3$ S–scheme heterojunction with rich oxygen vacancies for efficient and long–period CO_2 photoreduction in liquid–phase H_2O environment. Chem. Eng. J. **430**, 132820 (2022). https://doi.org/10.1016/j.cej.2021.132820
135. Q. Chen, X. Lan, K. Chen, Q. Ren, J. Shi, Construction of $WO_3/CsPbBr_3$ s-scheme heterojunction *via* electrostatic self-assembly for efficient and long-period photocatalytic CO_2 reduction. J. Colloid Interf. Sci. **616**, 253–260 (2022). https://doi.org/10.1016/j.jcis.2022.02.044
136. Y. Wang, H. Fan, X. Liu, J. Cao, H. Liu et al., 3D ZnO hollow spheres-dispersed $CsPbBr_3$ quantum dots S-scheme heterojunctions for high-efficient CO_2 photoreduction. J. Alloys Compd. **945**, 169197 (2023). https://doi.org/10.1016/j.jallcom.2023.169197
137. Z. Dong, Y. Shi, Y. Jiang, C. Yao, Z. Zhang, *In situ* growth of $CsPbBr_3$ quantum dots in mesoporous SnO_2 frameworks

as an efficient CO_2-reduction photocatalyst. J. CO2 Util. **72**, 102480 (2023). https://doi.org/10.1016/j.jcou.2023.102480

138. Z. Dong, J. Zhou, Z. Zhang, Y. Jiang, R. Zhou et al., Construction of a p–n type S-scheme heterojunction by incorporating $CsPbBr_3$ nanocrystals into mesoporous Cu_2O microspheres for efficient CO_2 photoreduction. ACS Appl. Energy Mater. **5**(8), 10076–10085 (2022). https://doi.org/10.1021/acsaem.2c01760
139. K. Su, S.-X. Yuan, Y.-X. Feng, G.-X. Dong, Y.-F. Mu et al., Polymer-assisted in situ growth of $Cs_3Sb_2Br_9$ on Co_3O_4 to boost sacrificial-agent-free photocatalytic CO_2 reduction. Rare Met. **44**(5), 3194–3205 (2025). https://doi.org/10.1007/s12598-024-02968-3
140. X. Kong, Q. Liu, C. Zhang, Z. Peng, Q. Chen, Elemental two-dimensional nanosheets beyond graphene. Chem. Soc. Rev. **46**(8), 2127–2157 (2017). https://doi.org/10.1039/c6cs00937a
141. T. Chai, X. Li, T. Feng, P. Guo, Y. Song et al., Few-layer bismuthene for ultrashort pulse generation in a dissipative system based on an evanescent field. Nanoscale **10**(37), 17617–17622 (2018). https://doi.org/10.1039/C8NR03068E
142. S. Wu, Z. Xu, J. Zhang, M. Zhu, Recent progress on metallic bismuth-based photocatalysts: synthesis, construction, and application in water purification. Sol. RRL **5**(11), 2100668 (2021). https://doi.org/10.1002/solr.202100668
143. Y. Zhang, Y. Tian, W. Chen, M. Zhou, S. Ou et al., Construction of a bismuthene/$CsPbBr_3$ quantum dot S-scheme heterojunction and enhanced photocatalytic CO_2 reduction. J. Phys. Chem. C **126**(6), 3087–3097 (2022). https://doi.org/10.1021/acs.jpcc.1c10729
144. Y. Feng, D. Chen, Y. Zhong, Z. He, S. Ma et al., A lead-free 0D/2D $Cs_3Bi_2Br_9/Bi_2WO_6$ S-scheme heterojunction for efficient photoreduction of C_O2. ACS Appl. Mater. Interfaces **15**(7), 9221–9230 (2023). https://doi.org/10.1021/acsami.2c19703
145. J. Wang, H. Cheng, D. Wei, Z. Li, Ultrasonic-assisted fabrication of $Cs_2AgBiBr_6/Bi_2WO_6$ s-scheme heterojunction for photocatalytic CO_2 reduction under visible light. Chin. J. Catal. **43**(10), 2606–2614 (2022). https://doi.org/10.1016/S1872-2067(22)64091-9
146. W. Huang, Q. Zhu, Z. Li, Y. Zhu, J. Shen, Construction of S-scheme $Cs_2AgBiBr_6/BiVO_4$ heterojunctions with fast charge transfer kinetics toward promoted photocatalytic conversion of CO_2. Small **21**(20), 2412289 (2025). https://doi.org/10.1002/smll.202412289
147. H. Bian, D. Li, S. Wang, J. Yan, S.F. Liu, 2D–C_3N_4 encapsulated perovskite nanocrystals for efficient photo-assisted thermocatalytic CO_2 reduction. Chem. Sci. **13**(5), 1335–1341 (2022). https://doi.org/10.1039/d1sc06131c
148. M.-R. Zhang, Y.-X. Feng, Z.-L. Liu, K. Su, S.-X. Yuan et al., A versatile self-templating approach for constructing ternary halide perovskite heterojunctions to achieve concurrent enhancement in photocatalytic CO_2 reduction activity and stability. Adv. Funct. Mater. **35**(22), 2423656 (2025). https://doi.org/10.1002/adfm.202423656
149. W. Huang, B. Chan, Y. Yang, P. Chen, J. Wang et al., Intermarrying MOF glass and lead halide perovskites for artificial photosynthesis. J. Am. Chem. Soc. **147**(4), 3195–3205 (2025). https://doi.org/10.1021/jacs.4c12619
150. T. Zhao, D. Li, Y. Zhang, G. Chen, Constructing built-in electric field within $CsPbBr_3$/sulfur doped graphitic carbon nitride ultra-thin nanosheet step-scheme heterojunction for carbon dioxide photoreduction. J. Colloid Interf. Sci. **628**, 966–974 (2022). https://doi.org/10.1016/j.jcis.2022.08.008
151. X. Feng, H. Ju, T. Song, T. Fang, W. Liu et al., Highly efficient photocatalytic degradation performance of $CsPb(Br_{1-x}Cl_x)_3$-Au nanoheterostructures. ACS Sustain. Chem. Eng. **7**(5), 5152–5156 (2019). https://doi.org/10.1021/acssuschemeng.8b06023
152. Z. Zhang, Y. Liang, H. Huang, X. Liu, Q. Li et al., Stable and highly efficient photocatalysis with lead-free double-perovskite of $Cs_2AgBiBr_6$. Angew. Chem. Int. Ed. **58**(22), 7263–7267 (2019). https://doi.org/10.1002/anie.201900658
153. Y. Zhao, Y. Wang, X. Liang, H. Shi, C. Wang et al., Enhanced photocatalytic activity of Ag-$CsPbBr_3$/CN composite for broad spectrum photocatalytic degradation of cephalosporin antibiotics 7-ACA. Appl. Catal. B Environ. **247**, 57–69 (2019). https://doi.org/10.1016/j.apcatb.2019.01.090
154. T. Paul, D. Das, B.K. Das, S. Sarkar, S. Maiti et al., $CsPbBrCl_2$/g-C_3N_4 type II heterojunction as efficient visible range photocatalyst. J. Hazard. Mater. **380**, 120855 (2019). https://doi.org/10.1016/j.jhazmat.2019.120855
155. Y. Wang, L. Luo, Z. Wang, B. Tawiah, C. Liu et al., Growing poly(norepinephrine) layer over individual nanoparticles to boost hybrid perovskite photocatalysts. ACS Appl. Mater. Interf. **12**(24), 27578–27586 (2020). https://doi.org/10.1021/acsami.0c06081
156. Z. Xue, P. Yan, A. Aihemaiti, A. Tuerdi, A. Abdukayum, Lead-free double halide perovskite Cs_2AgBiI_6/g-C_3N_4 heterojunction photocatalysts for effective visible-light photocatalytic activity. J. Solid State Chem. **348**, 125355 (2025). https://doi.org/10.1016/j.jssc.2025.125355
157. H. Huang, H. Yuan, J. Zhao, G. Solís-Fernández, C. Zhou et al., $C(sp^3)$–H bond activation by perovskite solar photocatalyst cell. ACS Energy Lett. **4**(1), 203–208 (2019). https://doi.org/10.1021/acsenergylett.8b01698
158. Z.-J. Bai, S. Tian, T.-Q. Zeng, L. Chen, B.-H. Wang et al., $Cs_3Bi_2Br_9$ nanodots stabilized on defective BiOBr nanosheets by interfacial chemical bonding: modulated charge transfer for photocatalytic $C(sp^3)$–H bond activation. ACS Catal. **12**(24), 15157–15167 (2022). https://doi.org/10.1021/acscatal.2c04652
159. W. Zhang, Y. Chen, X. Wang, X. Yan, J. Xu et al., Formation of n–n type heterojunction-based tin organic–inorganic hybrid perovskite composites and their functions in the photocatalytic field. Phys. Chem. Chem. Phys. **20**(10), 6980–6989 (2018). https://doi.org/10.1039/c7cp07819f
160. B.-M. Bresolin, P. Sgarbossa, D.W. Bahnemann, M. Sillanpää, $Cs_3Bi_2I_9$/g-C_3N_4 as a new binary photocatalyst for efficient visible-light photocatalytic processes. Sep. Purif. Technol. **251**, 117320 (2020). https://doi.org/10.1016/j.seppur.2020.117320
161. J.-R. Xue, R.-C. Xue, P.-Y. Chen, Y. Wang, L.-P. Yu, Novel hydrostable Z-scheme Ag/$CsPbBr_3$/Bi_2WO_6 photocatalyst for

 https://doi.org/10.1007/s40820-025-01886-y

effective degradation of Rhodamine B in aqueous solution. J. Chin. Chem. Soc. **70**(7), 1481–1492 (2023). https://doi.org/10.1002/jccs.202300025

162. Y. Zhao, X. Liang, X. Hu, J. Fan, Green and efficient photodegradation of norfloxacin with $CsPbBr_{3-r}GO/B_{i2}WO_6$ s-scheme heterojunction photocatalyst. Colloids Surf. A, Physicochem. Eng. Aspects **626**, 127098 (2021). https://doi.org/10.1016/j.colsurfa.2021.127098
163. E. Zhu, Y. Zhao, Y. Dai, Q. Wang, Y. Dong et al., Heterojunction-type photocatalytic system based on inorganic halide perovskite $CsPbBr_3$. Chin. J. Chem. **38**(12), 1718–1722 (2020). https://doi.org/10.1002/cjoc.202000333
164. Z.-J. Bai, Y. Mao, B.-H. Wang, L. Chen, S. Tian et al., Tuning photocatalytic performance of $Cs_3Bi_2Br_9$ perovskite by g-C_3N_4 for C(sp_3): H bond activation. Nano Res. **16**(5), 6104–6112 (2023). https://doi.org/10.1007/s12274-022-4835-z
165. Y. Teng, J.-H. Chen, Y.-H. Huang, Z.-C. Zhou, X.-D. Wang et al., Atom-triggered epitaxial growth of bi-based perovskite heterojunctions for promoting interfacial charge transfer. Appl. Catal. B Environ. **335**, 122889 (2023). https://doi.org/10.1016/j.apcatb.2023.122889
166. C. Callegari, C. Tedesco, A. Corbo, M. Prato, L. Malavasi et al., Application of lead-free metal halide perovskite heterojunctions for the carbohalogenation of C-C multiple bonds. Org. Lett. **27**(14), 3667–3672 (2025). https://doi.org/10.1021/acs.orglett.5c00780
167. Y. Zhong, H. Zhu, H. Zhang, X. Xie, L. Yang et al., Highly efficient photocatalytic synthesis of disulfides by a self-assembled $CsPbBr_3/Ti_3C_2T_x$ MXene heterojunction. Green Chem. **27**(19), 5455–5463 (2025). https://doi.org/10.1039/D5GC01214G
168. H. Huang, H. Yuan, K.P.F. Janssen, G. Solís-Fernández, Y. Wang et al., Efficient and selective photocatalytic oxidation of benzylic alcohols with hybrid organic–inorganic perovskite materials. ACS Energy Lett. **3**(4), 755–759 (2018). https://doi.org/10.1021/acsenergylett.8b00131
169. W. Wang, H. Huang, X. Ke, X. Liu, S. Yang et al., Morphology- and size-dependent $FAPbBr_3/WO_3$ Z-scheme photocatalysts for the controllable photo-oxidation of benzyl alcohol. Mater. Des. **215**, 110502 (2022). https://doi.org/10.1016/j.matdes.2022.110502